Post Access Report

Parametric Study of a Vertical-Axis Wave Turbine

Awardee: University of Texas Rio Grande Valley

Awardee point of contact: Yingchen Yang

Facility: American Bureau of Shipping

Facility point of contact: Shirlyn Zhang

Facility technical contact: Zhongfu Ge

Date: July 11, 2023

TEAMER
Testing & Expertise for Marine Energy

EXECUTIVE SUMMARY

In this study, different variates of the original geometry of the vertical-axis wave turbine (VAWT), designed by the University of Texas Rio Grande Valley (UTRGV), were generated and evaluated for hydrodynamic power efficiency using Computational Fluid Dynamics (CFD). The key geometrical parameters considered in this parametric study included the chord length of the rotor blades and the horizontal semi-axis length. The immersion depth of the rotor was also examined as a key deployment parameter for the wave turbine. The CFD simulation results revealed that a medium chord length of the blade (i.e., the same as that of the baseline design) and a shorter horizontal semi-axis for the guide curve of the blade than that of the baseline design resulted in higher hydrodynamic power to extract. With the most efficient turbine rotor geometry identified in this study, a deployment depth that could assure full submergence of the rotor in waves but as close to the free surface as possible led to a higher hydrodynamic power.

These findings revealed a pathway for the improvement of the wave turbine energy efficiency. The present parametric study will also lay the groundwork for a more sophisticated design optimization in future phases.

1 INTRODUCTION TO THE PROJECT

A novel wave energy converter (WEC), a vertical-axis unidirectional wave turbine, has been designed and preliminarily tested in a wave flume at the University of Texas Rio Grande Valley (UTRGV). Upon a successful validation of the proof of concept and demonstration of the power efficiency, UTRGV now seek TEAMER support to carry out Computational Fluid Dynamics (CFD) study of the turbine in waves for hydrodynamic optimization.

The turbine consists of a rotor, a vertical shaft, and a direct-drive electric generator. Figure 1 shows a wave farm that is comprised of multiple such turbines. When mounted to a floating platform and exposed in waves, the turbine performs unidirectional rotations about its vertical shaft to generate electricity. The turbine's rotor has a number of curved blades arranged like a Darrieus-type wind turbine. The detailed profiles of the individual blades, however, are largely different from those of the Darrieus wind turbine. Such differences are crucial in addressing the significantly different flow conditions between waves and winds.

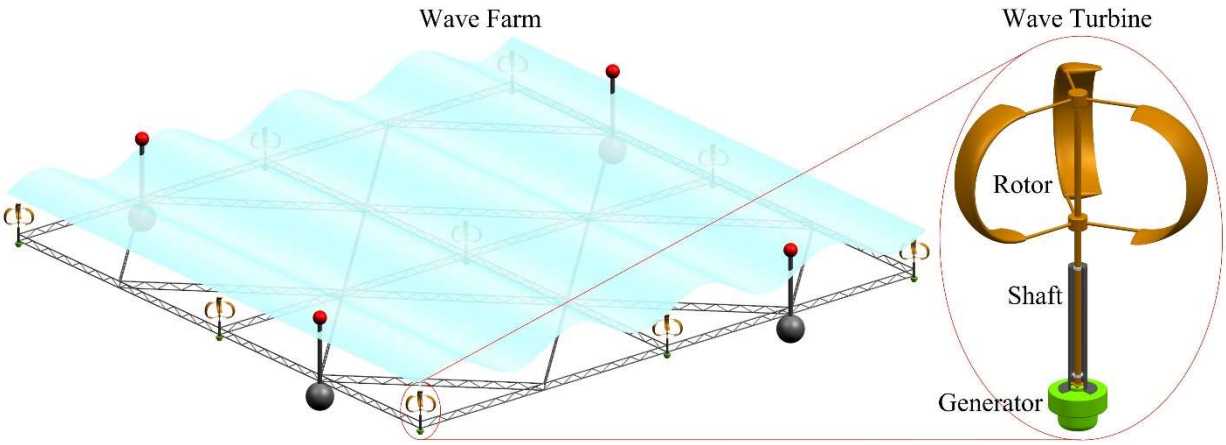

Figure 1. The proposed wave turbine (right) and its envisioned future application in a wave farm (left).

This project will be assisted by the Facility, American Bureau of Shipping (ABS), for energy efficiency evaluation and improvement of the turbine geometry using Computational Fluid Dynamics (CFD). With the allowed budget, the design optimization will be accomplished by a parametric study of the key geometric parameters including the chord length of the turbine's rotor blade sections, the guide curve contour of the rotor blades, and the immersion depth of the rotor. The objective of this study is maximization of the turbine power coefficient. Throughout the project period, UTRGV will provide technical guidance on the acceptance criteria of the turbine power performance, the allowable ranges of the geometrical parameters, the damping torque as a function of the turbine rotational speed, and the interpretation of the CFD results from the design perspective. Unlike a global optimization of a design which searches for an optimal solution in a large design space, our proposed parametric study only involves CFD calculation of the hydrodynamic performance of each pre-determined variate of the baseline design. This approach is not expected to lead to an exact, optimal solution, but it will provide invaluable insight into the directions for design modification. In a future phase, a full optimization guided by

sophisticated search algorithms can be attempted based on what has been learned from the present project.

2 ROLES AND RESPONSIBILITIES OF PROJECT PARTICIPANTS

2.1 APPLICANT RESPONSIBILITIES AND TASKS PERFORMED

UTRGV will provide the complete 3D model of the WEC to be used as the baseline design for the present study. The 3D CAD model should be suitable for CFD modeling with minimum labor for geometry checking and cleaning. Along with the CAD model, UTRGV will also provide a document detailing the specific values of the key parameters, including but not limited to the rotor dimensions, the blade section parameters, the guide curve formula, and the cambering formula of the blades along their respective guide curves. If the original geometry needs simplification, the simplification strategy will be decided by both UTRGV and ABS.

UTRGV will provide a counter-torque curve, i.e., the torque versus the RPM (revolution per minute) of the rotor, to represent the instantaneous loss of kinetic energy due to the frictions in the mechanical system and the Power-Take-Off (PTO). ABS will test different torque curve options. UTRGV will be responsible for selecting a reasonable one before the parametric study begins.

Since self-starting is an important aspect of this type of wave turbines, CFD will be used to simulate the transient start-up process. To this end, the detailed mass properties and distribution of the rotor will be provided by UTRGV.

Throughout this project, there will be frequent communications between the two parties mostly in the form of virtual meetings to discuss the numerical results as they become available.

2.2 NETWORK FACILITY RESPONSIBILITIES AND TASKS PERFORMED

ABS, as the network facility, will provide design parametric study using CFD, deliver results summary and recommendations to the Applicant. ABS' key tasks are as follows:

- Discuss with the Applicant about the baseline design, parameterization strategies, parameter constraints, objective function, counter-torque curve options, and the ambient flow conditions, such as the length and height of the regular waves to be used
- Set up a CFD model for a 3-blade baseline design
    - Conduct CFD model time-step and grid convergence testing
    - Evaluate the power output of the baseline design
    - Evaluate the influence of the different counter-torque curves
    - Settle on a torque curve for all subsequent cases
- Vary the chord length of the rotor blades and the guide curves for each blade and run CFD for each design variate
    - Identify the best combination of the chord length and guide curve
- Vary the immersion depth and run CFD for each condition
    - Identify the best rotor immersion level

- Compare the power coefficients of all designs examined
- Report findings

3 PROJECT OBJECTIVES

The overall assistance goal is to improve the WEC hydrodynamic efficiency by finding better geometrical parameters for the turbine rotor using high-fidelity CFD modeling. A significant wave height of 1.75 m and a dominant wave period of 8.5 s, which are the most common (~528 hours per year) in the PacWave open water test site 7 miles off the coast of Newport, Oregon, will be used for the CFD analysis. The corresponding dominant wavelength is 112.8 m. Due to the limited time frame, an equivalent regular wave, with the same dominant wave period and a wave height jointly determined by UTRGV and ABS, will be used for the preliminary design purpose. Only a three-blade rotor configuration in a regular wave environment will be considered in this study. Individual rotor blades will be created by sweeping and gradually cambering (in a predefined way) an originally symmetric NACA0021 hydrofoil along a guide curve. The baseline design will have a semicircular guide curve.

The specific technical assistance objectives are as follows:

1. To parameterize the WEC's geometrical configuration for the proposed parametric study; the geometrical parameters will include, e.g., the number of blades, the section profiles of the blades, the definition of the guide curve, the blade cambering along the guide curve, and the other main dimensions of the WEC
2. To determine an optimal turbine design/configuration with the maximum power output based on the geometrical parameters examined

This project will focus on the hydrodynamic performance of the turbine in a regular wave environment. The key performance indicators will include:

- The torque coefficient of the turbine
- The power coefficient of the turbine

The optimization of the turbine design will have a large influence on the LCOE of these turbines later in production. The volumetric flow rate will determine the amount of the kinetic energy the rotor can extract from the ambient flow and will in turn affect the LCOE. It is anticipated that we can increase the efficiency of this WEC design to 20% to 40% higher than that of the baseline design.

4 TEST FACILITY, EQUIPMENT, SOFTWARE, AND TECHNICAL EXPERTISE

Overall expertise of ABS

ABS is a not-for-profit marine classification, standards, and technology organization in the U.S. ABS has over 3,000 engineers, scientists, and marine surveyors with global expertise related to the design, installation, operation, and maintenance of marine and offshore assets. ABS completes multiple research

and development projects per year on CFD applications to ship and offshore topics (e.g., wave and current loads on marine structures/assets).

Simulation and data analysis software

ABS has considerable experience in general CFD software such as OpenFOAM. For the present project, ABS will use OpenFOAM (also referred to as "ABSFoam"), which has been enhanced and secondary-developed for marine and offshore applications. Hexpress (NUMECA International) will be used for mesh generation. CFD post-processing or visualization is implemented by Paraview. Data analysis will be carried out by numerous Python scripts developed for routine CFD needs.

Simulation hardware

ABS has its in-house High-Performance Computing (HPC) hardware, including three clusters with a total of more than 1,000 cores. ABS HPC is managed daily by a professional IT team that supports the entire company.

ABS key personnel expertise

ABS' numerical simulation work will be managed by Dr. Zhongfu Ge, Manager of Technology, and supported by a Senior CFD Engineer. Dr. Ge has been leading ABS' global CFD capabilities for more than six years and has extensive experience in solving industrial problems using CFD. He also has been Principal Investigator or co-Principal Investigator for several government-funded projects. The ABS team has experience in similar projects (CFD analysis for WECs and current turbines) supported through TEAMER, which assures success for the present project.

5 TEST OR ANALYSIS ARTICLE DESCRIPTION

The WEC to be examined in the present project is a vertical-axis unidirectional wave turbine. The basic configuration of the WEC has been described in Section 1 "Introduction to the Project". The WEC configuration is similar to those of vertical-axis wind turbines, but in terms of the dynamics it is significantly different.

For vertical-axis wind turbines, a unidirectional steady flow is often assumed for design purposes. In waves, however, water particles will move in orbital motions with Stokes drifts. The flow conditions will become even more complex in irregular waves. Hence, omnidirectional unsteady flows must be considered in wave turbine designs. To achieve a unidirectional rotation for the proposed wave turbine in such omnidirectional flows, two conditions must be met. First, the spanwise curving of the individual blades and the sectional cambering of the hydrofoils at various blade cross sections need to be carefully designed. This way, no matter what direction the local water is moving, it can always drive the rotor in one direction only. Second, the rotor's swept diameter needs to be small enough compared to the dominant wavelength. With that, the local flow in a region comparable to the rotor size is relatively uniform (spatially, but not temporally) in the absence of the rotor. In meeting these two conditions, UTRGV's initial success through preliminary wave flume testing encouraged the project team to advance

the wave turbine development by means of numerical modeling and optimization as the next-step approach.

UTRGV's wave turbine concept is also fundamentally different from most WEC technologies being explored nowadays. In general, a majority of WECs perform reciprocating motions in waves, e.g., heaving up and down, swaying back and forth, or bending/curving periodically. The reciprocating motions demand the WEC to rely on a certain resonance mechanism to achieve a high power efficiency (capture width ratio). Since the dominant wave frequency in the natural ocean environment changes from time to time, it is highly desired that the WEC has a frequency-tuning capability to broaden the frequency range for resonance. Unfortunately, no frequency-tuning technology has proven to be implementable so far, due to the complexity and/or high costs. Another challenge is that many WECs must be aligned with the wave propagation direction for normal operations. WEC realignment to cope with the changing wave directions could be very difficult or very costly to realize, particularly in a wave farm with an array of WECs.

In contrast, the proposed wave turbine naturally circumvents the above two challenges. The turbine's rotor performs unidirectional rotations about a vertical axis for power generation. The turbine-typed configuration allows the WEC to operate under a broad range of wave frequencies since it does not rely on the resonance principle. The vertical-axis configuration makes the turbine insensitive to the wave direction since waves from any direction would act on the rotor in the same way. This wave turbine concept augments the marine energy sector with a new WEC technology. Its simple structural setup and its broad operational range demonstrate a great potential for low-cost electricity production. From a scientific perspective, using a single direction flow to drive a rotor for unidirectional rotation has been well demonstrated (e.g., all horizontal-axis wind turbines). Using a bidirectional flow to drive a rotor into a unidirectional rotation is less common but has been realized as well (e.g., Well's turbines). Using an omnidirectional flow to drive a rotor into a unidirectional rotation (the present research), however, has never been reported for WECs in the literature by other researchers to the best of our knowledge.

For the baseline rotor configuration, a scaled rotor model has been 3D-printed, assembled, and tested in a wave flume at UTRGV (Figure 2, left). Three identical rotor blades were created by sweeping a changing cross-section along a semicircular guide curve with a radius of 0.127 m. The thickness of the hydrofoil remained at 0.027 m in sweeping. At the two spanwise ends of the blades, the hydrofoil had a symmetric NACA0021 profile (i.e., zero-chambering there). In the mid-section of the blades spanwise, the hydrofoil became the NACA0021 cambered at a radius of 0.237 m. The chambering gradually changed from the ends toward the mid-section along the span. The assembled rotor had a swept diameter of 0.5 m and a height of 0.281 m.

The rotor was tested by UTRGV in a wave with a realized wave height of 0.22 m and a wave frequency of 0.5 Hz. A rotary encoder was employed to measure the rotor's angular velocity in real time. Under a freewheeling condition, an angular velocity time trace over 20 wave cycles demonstrated a unidirectional rotation of the rotor (Figure 2, right). More data were obtained under various test conditions (e.g., with a flywheel to reduce the fluctuations in the angular velocity, with a damping torque to mimic the Power Take-Off, etc.). The test results supported the wave turbine concept proposed herein.

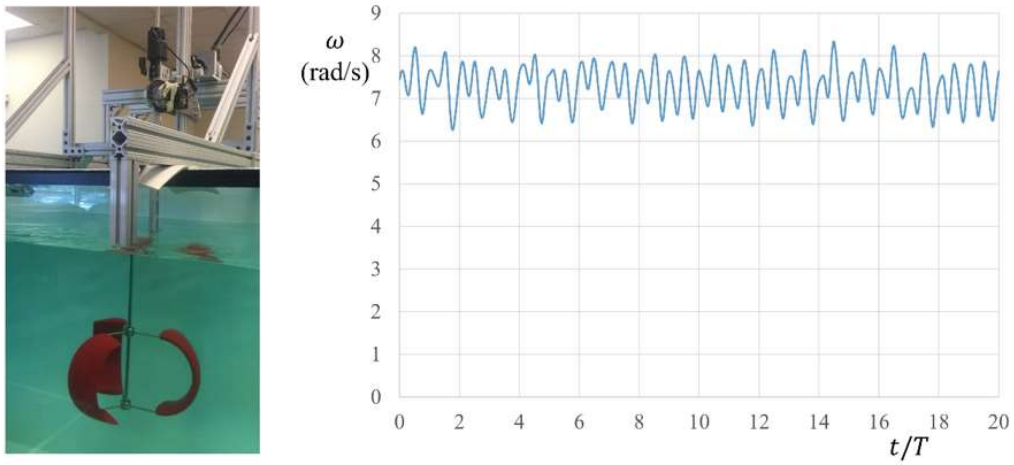

Figure 2. Experimental setup (left) and a time trace of the rotor's angular velocity in waves (right) of a previous wave flume testing.

To move forward with the wave turbine design, CFD analysis became a logical next step. With the TEAMER support for this numerical work, we expect to: (i) gain in-depth understanding on wave-rotor interactions, (ii) quantify the rotor power performance in waves, and (iii) achieve a set of optimal rotor design parameters. After this work is completed, the Applicant will adopt the identified optimal design parameters and build a new scaled prototype of the wave turbine for further testing. The Applicant hopes to investigate the prototype systematically at a Test Facility in the TEAMER network. Without the CFD work proposed herein, it is not possible to tank-test a large number of candidate designs.

6 Work Plan

6.1 Numerical Model Description

ABS will use a high-fidelity CFD model based on 3D Reynolds-Averaged Navier-Stokes (RANS) equations, supplemented by a $k-\omega$ SST turbulence model (Omar et al., 2018). The governing equations will be discretized by the Finite Volume Method. Regular waves will be generated. The free water surface will be resolved using the Volume of Fluid (VOF) method. The flow field will consist of two phases: the liquid phase (i.e., the water) and the gas phase (i.e., the air). In waves, the rotor is assumed to have one degree of freedom only: rotation about the shaft. The computational domain will be discretized into unstructured grids, with various refinement zones for the areas where flow properties are expected to change rapidly. Viscous layers (or prism layers) will be generated around solid walls to resolve boundary layers. Wall functions will be used for calculating the flow dynamics in the boundary layers. A dynamic overset grid will be created for the rotor (turbine blades and the shaft) domain. The overset grid domain will be assembled with the stationary background domain. The simulation will be unsteady. ABS will monitor time histories of the force components and the total torque applied to the rotor until they reach a steady, oscillatory state.

ABS will use OpenFOAM as the CFD platform, which has been enhanced and secondary-developed for marine and offshore applications (informally referred to as "ABSFoam"). Hexpress will be used for mesh generation. CFD post-processing is partially done within the OpenFOAM model and partially implemented with a separate software tool, Paraview. All flow visualization is performed by Paraview.

For the time-step and grid-size convergence testing, a matrix of three different grid-size levels (for example, fine, medium, and coarse) by three different time-step levels (for example, small, medium, and large) will be used for the baseline design. The best grid-size and time-step strategy will be determined to achieve economy and converged accuracy. Moreover, as the parametric study will involve small local changes in the geometries, the use of consistent computational grids will be critical. We plan to only make local changes to the grids for each design variate, wherever applicable. The overall grid structures should remain as consistent as possible across different designs.

In addition to the dedicated time-step and grid-size testing, ABS has conducted numerous validation studies in the past years. For this particular project, CFD results could also be compared with the existing results obtained by the Applicant from experiments. Such comparisons will help increase confidence in the validity of the CFD models.

6.2 Test and Analysis Matrix and Schedule

Figure 3 shows the definition of the rotor blade geometry. Overall, the rotor is axisymmetric about the shaft. We have set the number of rotor blades to three for simplicity. The rotor blade section will be provided by the Applicant, including the symmetric NACA0021 profile and the pre-defined cambering strategy along the guide curve.

For this phase of development, we are not aiming to do a full-blown optimization with advanced search algorithms. With the limited time and budget, ABS will carry out a simplified parametric study in order to identify the general directions for improving power output. The best design identified in the end will not necessarily be the global optimal design in a broad sense. However, the results should be able to show the correct directions for improvement.

The CFD-based parametric study will focus on the variations of three geometric parameters, namely,

- The blade chord length
- The horizontal semi-axis length (b as in Figure 3) of the guide curves
- The rotor immersion depth.

For this exploratory study, we will defer the variation of other blade section parameters (such as the chamber and the thickness distributions) to future phases. When changing the blade section chord length, the other key parameters will remain unchanged. A total of 3 levels of chord lengths will be investigated, i.e., 0.7, 1.0, and 1.3 times the original value. The guide curve of the blade has a semielliptical segment in the middle and straight segments at the top and bottom, respectively (Figure 3). The semielliptical segment has a vertical semi-axis a and a horizontal semi-axis b. In varying the guide curve shape, we will maintain a (with $2a$ representing the rotor height) and R (with $2R = D$ representing the rotor diameter)

as well as the overall arc length of the guide curve (the part in red in Figure 3), while varying the value of b (resulting in changes in the two straight segment length, c). With the challenging CFD modeling required for the present project (i.e., self-started turbine motion and the wave dynamics), we will vary b into four different levels: 1.2, 1.0, 0.8, and 0.6 times the value a. The CFD analysis will be conducted for a two-way matrix considering the different chord lengths and different guide curve shapes together. This will result in a total of 3 x 4 = 12 cases.

When investigating the effect of the immersion depth on the turbine power performance, we will adopt the best design (with the highest power output) from the previous step and test four different immersion levels: 0.5, 1.0, 1.5, and 2.0 times $2a$, i.e., the rotor height, below the calm water surface.

In general, it is difficult to predict which direction of changes of the design parameters will lead to better designs. The levels of variations could be adjusted during the execution of the project.

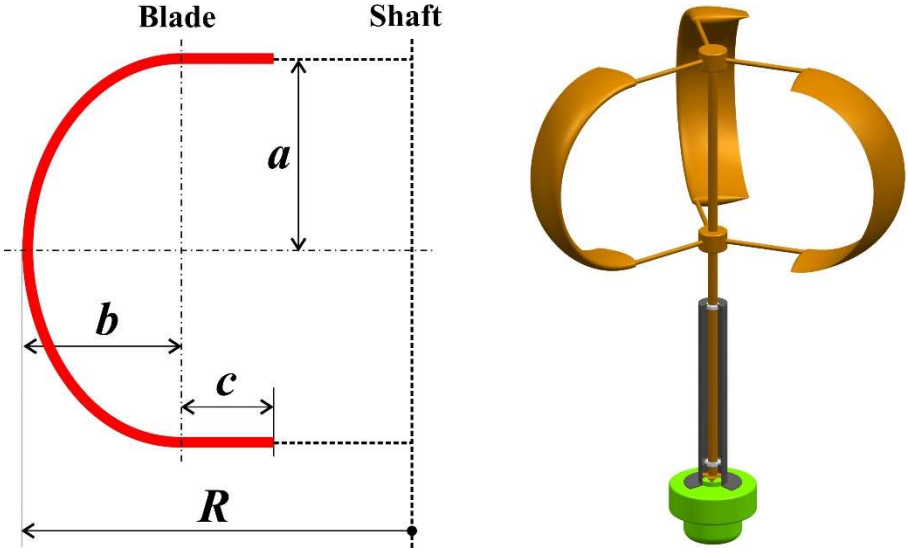

Figure 3. Definition of the wave turbine's rotor blade geometry.

Following the reasoning above, we summarize the specific tasks and the proposed schedule in Table 1. During the project execution, some design changes could be omitted if similar changes have shown negligible improvements in the power performance. The decision on omitting any case will be proposed by ABS and agreed to by UTRGV. This flexibility is allowed due to the anticipated long computational time for each CFD case which involves turbine self-starting.

At the end of Tasks D and E as in Table 1, the best design up to that point will be recommended and enter the next task. ABS will seek agreement from UTRGV on the milestone design.

Table 1. Break-down of project tasks, the number of cases, and timeline for each task.

Task	Case details	Number of cases	Time cost (week)	Note
A. Grid-size time-step convergence test	Test baseline design with a 3 x 3 grid-size and time-step matrix	9	6	The best setup will be adopted for next tasks
B. Damping torque curves testing	Test two more damping torque curves on the baseline design	2	1.5	Settle on one damping torque curve for all subsequent cases
C. Test the Rhinoceros3D automated geometry generation script	The script is intended to automate the geometry generation of the main part of the turbine as shown in Figure 3	N/A	1.5	
D. CFD for combinations of chord length and horizontal semi-axis b of the guide curve	3 chord lengths; 4 horizontal semi-axis levels	12	8	Only the best design proceeds to next steps
E. CFD for different immersion levels	3 additional immersion levels	3	2	Only the best design proceeds to next steps
G. Summary of power performance for all designs	Present the comparison of power performance for all designs investigated	N/A	1	
H. Reporting	Final report		2	
Total		26	22	

6.3 SAFETY

The mission of ABS is to serve the public interest as well as the needs of our clients by promoting the security of life and property and preserving the natural environment. ABS is committed to excellence in environmental, health and safety management. ABS promotes a safe and healthy environment for staffs and visitors, through programs and practices designed to protect people and the environment.

The ABS staffs will follow all relevant safety procedures and protocols outlined on the ABS Health, Safety, Quality, Environmental (HSQE) SharePoint Site (internal access only).

6.4 CONTINGENCY PLANS

Manpower

ABS will have at least three qualified CFD modelers who can support the proposed project during the project time. The manpower will be more than sufficient to carry the project to completion.

Schedule

The project is budgeted for 600 man-hours based on ABS' rates. The planned project duration (i.e., 22 weeks as in Table 1) will be longer than 600 hours because of the long computational time anticipated.

Computation hardware

ABS has its in-house HPC resources. In the very rare scenario where internal resources become unavailable, ABS will use external resources such as those from the Texas Advanced Computing Center (TACC). ABS has an existing account with TACC and has used their service before. ABS will be responsible for any extra cost for using TACC.

6.5 Data Management, Processing, and Analysis

6.5.1 Data Management

During the project, ABS will provide a secure data management environment for collaborative work among project team members. Our team will store and maintain the data in the Microsoft (MS) Teams environment with integrated MS Office applications. Microsoft OneDrive will be used to keep data and files backed up, protected, synced, and accessible on all our devices. This OneDrive app lets us view and share OneDrive files and documents with all team members.

ABS' IT department maintains appropriate cybersecurity controls consistent with the U.S. Government Risk Management Framework for cybersecurity and other IT-security requirements. We will be glad to provide additional information on these controls as requested.

During CFD simulations, data will be stored in a dedicated directory on ABS' HPC cluster. In the OpenFOAM style, each case will have a separate case folder. Each case folder will contain different time folders, which store data for the entire flow field at the associated simulation time. The case folder will also contain separate output files, each containing certain flow variables being monitored every time step. Once a simulation is completed, post-processing scripts can be run for further integration or extraction of the raw output data. The resulting data files will also be saved under the main case folder.

For confidentiality, the project data will remain in-house between ABS and UTRGV. The data from which the graphics, tables, and charts are produced for the final report will be submitted to the MHK-DR, as required.

6.5.2 Data Processing

The following measures will be taken to monitor the data quality in run-time. The CFD software OpenFOAM has the capability of outputting average and maximum Courant number of the entire flow field, which altogether indicate the numerical stability of the simulation. Once the Courant numbers become too high, the simulation could be unstable. Other output files including a general log file and data files for monitoring the total thrust and total torque are updated on the fly every time step. The modeler

will inspect data trends frequently, following ABS' CFD best practices, to identify potential problems in the simulation as early as possible.

6.5.3 Data Analysis

The CFD models will always include various monitors of the flow conditions, either based on the raw data or on processed statistics. The following variables will be stored for the entire computational domain for every design examined. They will be stored at selected time instants after the steady state is attained.

- Three-dimensional velocity components
- Pressure
- Free water surface pattern
- Variable k as in the $k-\omega$ SST turbulence model
- Variable ω as in the $k-\omega$ SST turbulence model
- Eddy viscosity υ_t as output of turbulence model

The following variables will be stored for every time step throughout the simulation for each design examined:

- Total streamwise force on the turbine blades and on each blade separately
- Total cross-stream force on the turbine blades and on each blade separately
- Total torque about the shaft on the turbine blades and on each blade separately

Moreover, the following variables will be calculated and averaged for the steady state:

- Power coefficient
- Torque coefficient

Once a simulation is completed, the output time series, including forces and torque, will be plotted out and inspected. The final steady state will be identified. The turbine performance indicators for a particular design should always be based on the averages over this steady state. When performing time averaging, we always select full oscillation cycles in order to minimize the error.

After all design variates have been examined, the power coefficient of all cases will be demonstrated on the same graph for inspection and comparison.

Although it is well understood that every CFD simulation may have some uncertainty and errors, we will focus on the relative difference and improvement between designs. The uncertainties that are common to all cases will be minimized in the conclusion.

7 PROJECT OUTCOMES

7.1 RESULTS

7.1.1 CFD Model Setup

CFD model setup has been described in Section 6.1. Since the WEC was deployed near the free water surface, the free surface effect was considered in the CFD simulations by means of the Volume of Fluid (VOF) method. The rotor was assumed to be a rigid body. It took on a rotational motion around its central axis under the forcing from the waves. A damping torque with respective to the same axis, which counters the hydrodynamic torque, also should exist in the actual operations of the WEC. The damping torque is a resultant moment from any frictional losses in the rotor machinery setup or, more importantly, due to the rotor kinetic energy harnessed by the Power-Take-Off (PTO) unit. In CFD, the damping torque was simply applied to the rotor as an external moment T_g. The motion of the rotor is described by the equation

$$I \cdot \frac{d\Omega}{dt} + T_f + T_g = T_w \tag{1}$$

where I is the moment of inertia of the rotor, Ω is the angular velocity, and T_w is the hydrodynamic torque generated by the incident water flow (Liu et al., 2016). The system load consists of the friction load T_f (constant) and the resistive load from the PTO, T_g. For preliminary analysis, T_f can be omitted and T_g can be simplified as

$$T_g = k \cdot \Omega \tag{2}$$

where k is a constant (unit: Nms/rad). This is the simplification adopted in the present study.

Figure 4 illustrates the computational domain. The boundary conditions are described in Figure 4(a). The inlet boundary was where the incident waves entered the computational domain; the outlet boundary was set as a pressure outlet; the remaining four sides of the domain were free slip walls. The water depth was set to 70 m, as suggested by UTRGV. A dynamic overset grid technique was adopted to handle large and complex amplitudes in the motions, such as the rotation of the rotor. It helped avoid large mesh deformations which would be an issue for the traditional deforming mesh methods. As shown in Figure 4(b), the rotor of the WEC was inside an overset grid region. Figure 5 shows a perspective view of the background grid, including the surface mesh and volume mesh across the rotor axis. Two zones were locally refined for CFD simulations, including the zone encompassing the possible range of the free surface motion and the zone around the rotor in the overset region.

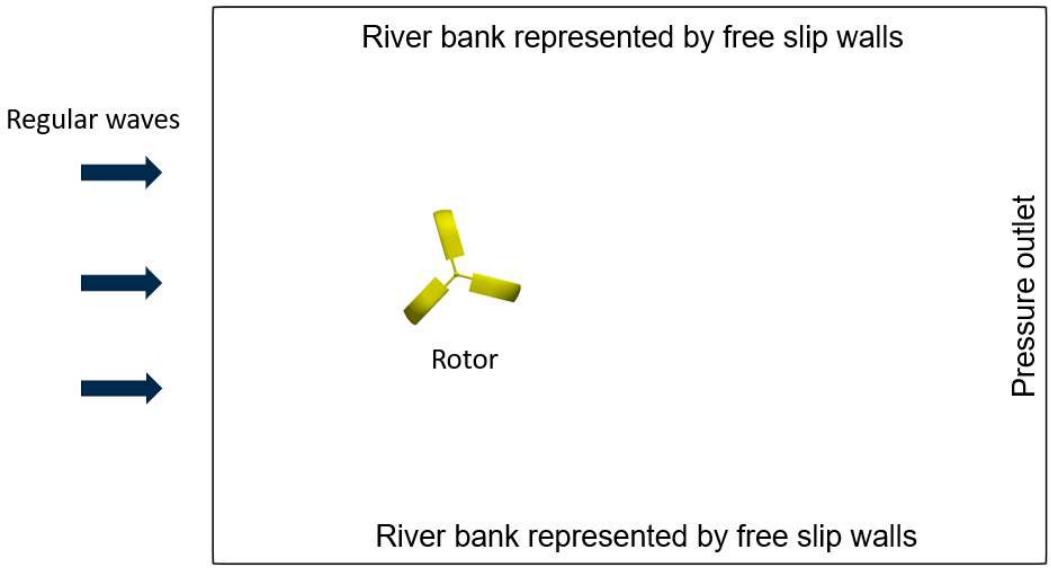

(a) Boundary conditions

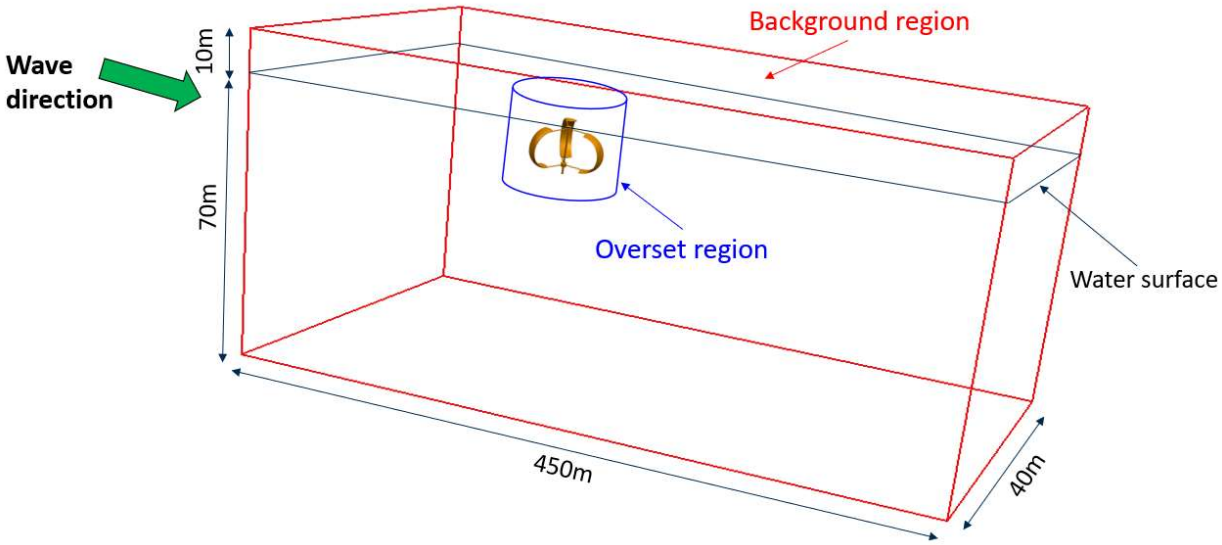

(b) Background region and overset region

Figure 4. The computational domain for the WEC: (a) Boundary conditions; (b) the background and the overset regions.

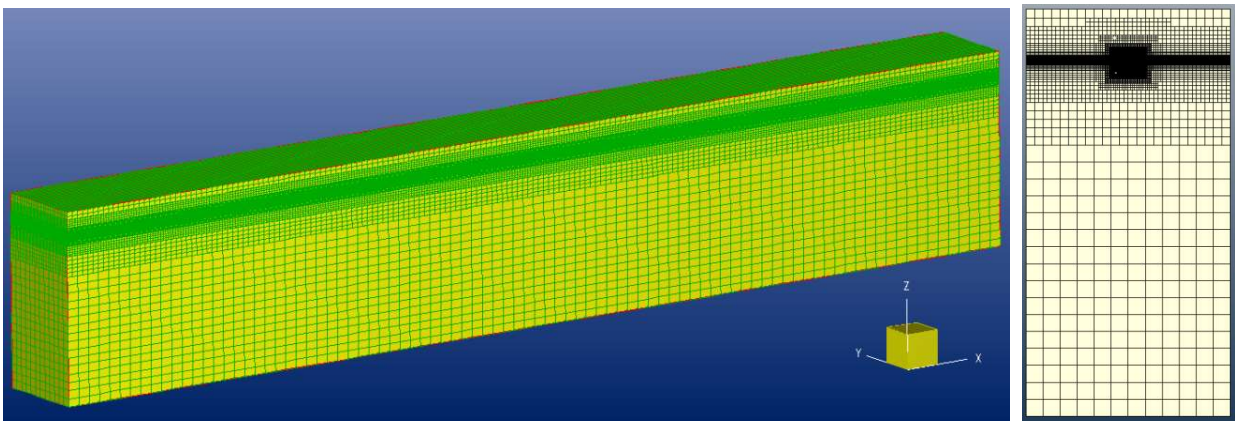

Figure 5. The surface mesh of background grid and volume mesh across the rotor axis.

Figure 6 shows the overset region around the rotor and its surface mesh for the WEC baseline design. Figure 7 presents the assembled volume mesh, consisting of the rotor (i.e., the overset) and the background grids. This computational grid is actually the medium grid as detailed in Section 7.1.2.

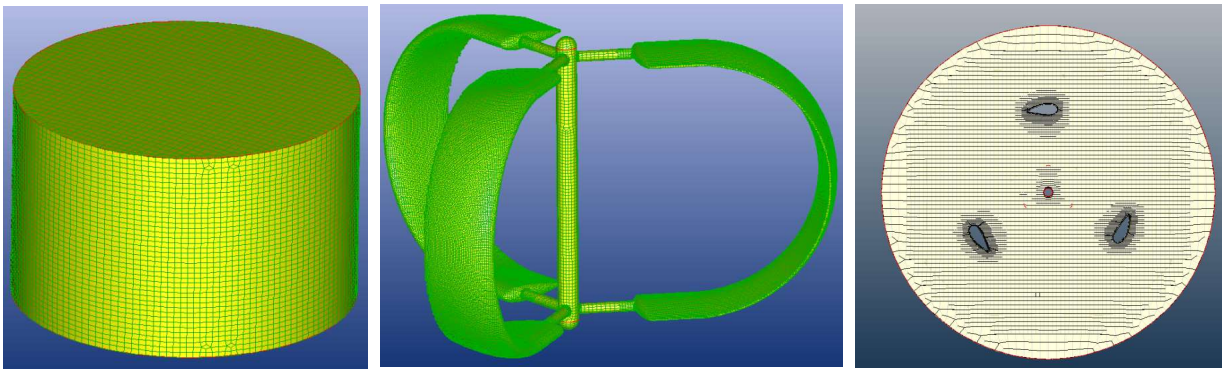

Figure 6. The computational mesh on the outer surface of the overset region (left), on the surface of the rotor (middle), mesh (left and middle) and in a horizontal plane that cuts across the rotor (right) for the baseline design.

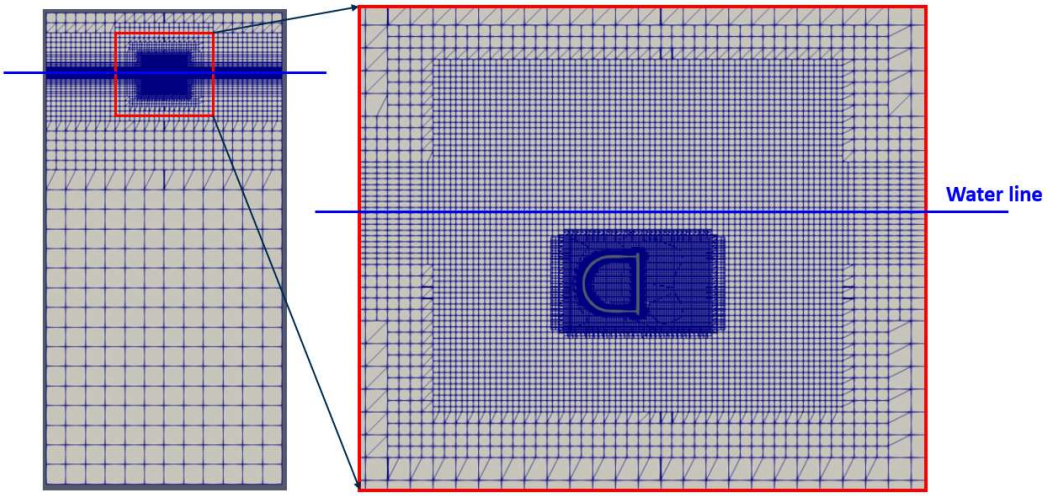

Figure 7. The assembled volume mesh as viewed in the plane at x = 0 (left) and a close-up view of around the rotor (right).

Regular waves were applied in the simulations with a wave height of 1.75 m and a wave period of 8.5 s. The corresponding wavelength was 112.8 m. This wave condition was provided by UTRGV as a typical design condition. Figure 8 presents the CFD-simulated wave pattern when the rotor is absent. In the first simulation cases, the rotor was positioned just beneath the trough of the original incident wave. This level of immersion was a typical design draft for the rotor. The simulation for the rotor self-starting process (Khalid et al., 2022; Zhu et al., 2022) was unsteady. The time histories of the force components and the total torque applied to the rotor were monitored to assure they reach a steady, oscillatory state.

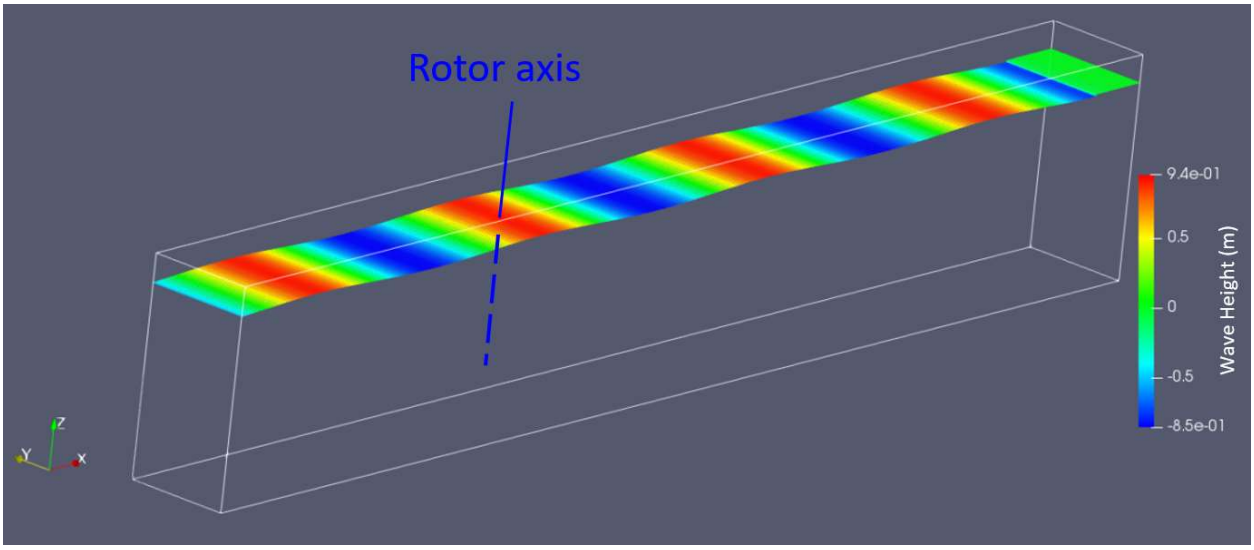

Figure 8. CFD-generated regular wave in the computational domain (wave height: 1.75 m; wave period: 8.5 s).

7.1.2 Convergence tests of CFD grids and time-steps

A convergence test for the time-step and grid-size was performed on a 3 by 3 matrix. The three grid-size levels were set based on the characteristic length L which is the rotor height (1 m):

- Coarse grid: 3.0 million cells (Δx = 0.055L)
- Medium grid: 4.2 million cells (Δx = 0.042L)
- Fine grid: 5.8 million cells (Δx = 0.034L)

where Δx is the minimum grid size for the refined mesh around the rotor. The volume meshes for the coarse, medium and fine level grids, respectively, around the WEC rotor are shown in Figure 9.

The three different time-step levels were based on the steady-state rotation period of the rotor, T, which was approximately 2.5 s:

- Δt = 0.005 s (0.002T)
- Δt = 0.01 s (0.004T)
- Δt = 0.02 s (0.008T)

For the purpose of convergence test, the rotor mass was assumed to be 300 kg and the corresponding

moment of inertia was approximately 120 kg·m^2. The damping coefficient for rotative motion was applied as 10 Nms/rad. Other values for the mass properties and the damping coefficient for rotation were further tested, and the results are presented in Sections 7.1.3 and 7.1.4.

The attained average RPMs (Revolutions Per Minute) for the corresponding steady states were compared for the cases in the grid size and time step matrix, as shown in Table 2. For Δt = 0.01 s, the time histories of the rotor instantaneous RPMs for the three sets of grids are shown in Figure 10. If the fine grid and a time step of 0.005 s presumably produced the most accurate result, its difference from the result using the reference combination, i.e., the medium grid and a time step of 0.01 s, was only 2.1%. This difference is acceptable. Therefore, we consider the results based on the reference grid size and time step to be converged and hence used the reference combination for all cases in the remainder of the parametric study.

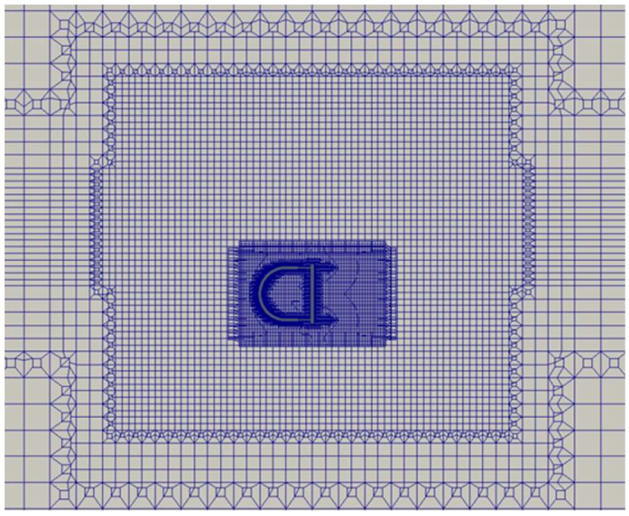

(a) Coarse grid

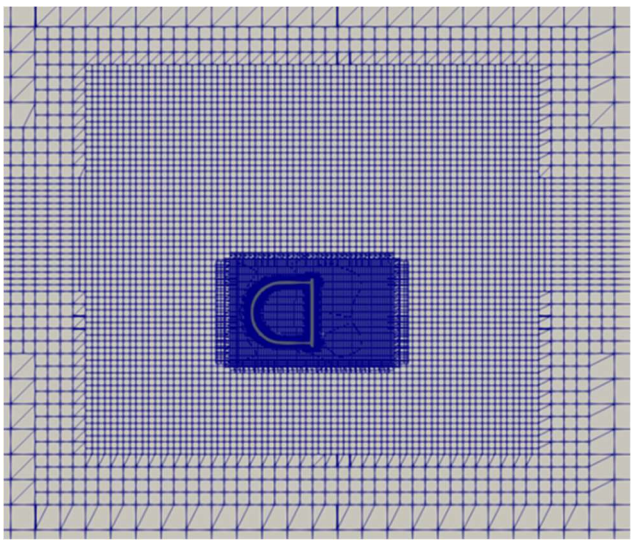

(b) Medium grid

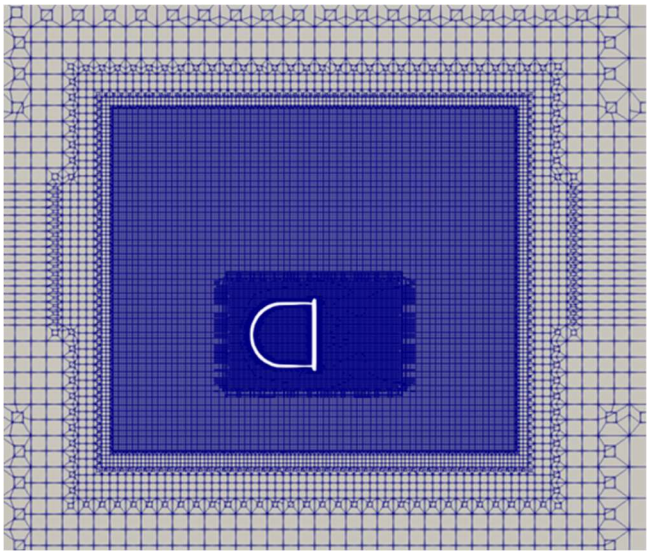

(c) Fine grid

Figure 9. Three different grid-size levels for the convergence tests on the baseline design: (a) Coarse grid; (b) Medium grid; and (c) Fine grid.

Table 2. The calculated average RPMs that the baseline rotor attained during the steady state using different combinations of grid size and time step as compared to that using the reference grid size and time step.

Difference in RPM (%)	Coarse Grid	Medium Grid	Fine Grid
Δt = 0.005 s	-8.8%	1.6%	2.1%
Δt = 0.01 s	-10.2%	0.0% (reference)	1.9%
Δt = 0.02 s	Diverged	-8.3%	-4.4%

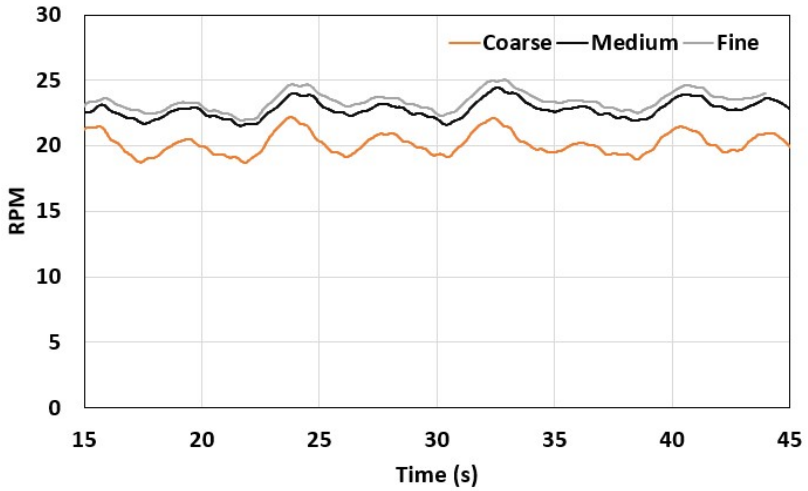

Figure 10. Instantaneous rotor RPM time histories for the coarse, medium, and fine grids and a time step of 0.01 s.

7.1.3 Test on the mass and moment of inertia of the rotor

Apart from the design geometry of the rotor, the mass properties including the total mass and the moment of inertia around the axis of rotation would be directly relevant to the rotor dynamics. Since at the current stage of design the material of the rotor had not been determined, different masses and moments of inertia of the rotor were investigated here to evaluate their influence on the rotor's dynamic performance. As detailed in Table 3, the rotor material was first assumed to have a uniform density the same as that of water (i.e., 1025 kg/m^3), which would result in a total mass of 88 kg for the rotor; the total mass of 300 kg was based on a uniform density close to that of the aluminum alloy, which was being considered as the material for the rotor fabrication. Two higher densities were also examined, leading to greater total masses of 500 kg and 700 kg, respectively. The moments of inertia around the rotational axis were estimated similarly based on a uniform material density.

Table 3. Total masses and their corresponding moments of inertia around the rotational axis examined in the CFD simulations.

Mass (kg)	**Moment of inertia (kg·m^2)**
88	35.2
300	120
500	200
700	280

For all mass properties examined here, the rotational damping coefficient was assumed to be 10 Nms/rad. Figure 11 presents the rotor angular velocity time histories covering the self-starting and steady-state periods for the four different rotor materials as in Table 3. It can be observed that a lighter rotor tended to have greater oscillatory ranges for the angular velocity. The self-starting process was the longest (i.e., about 20 s) for the rotor with the greatest total mass, i.e., 700 kg. In contrast, it took the lightest rotor, i.e., with a total mass of 88 kg, only about 8 s to spin up to a steady state. But all materials appeared to result in similar angular velocities averaged over the respective steady state periods. Therefore, the total mass of the rotor will only influence the efficiency of the self-starting process but not the average motion in the steady state.

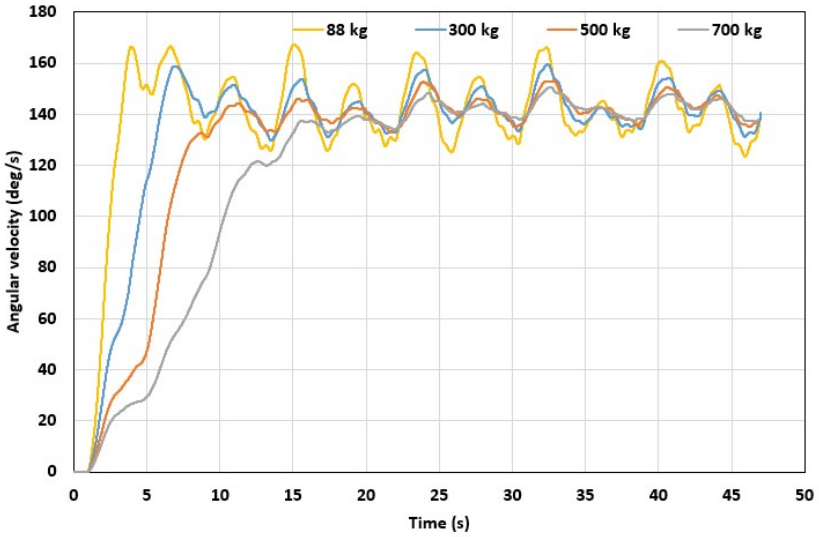

Figure 11. Rotor transient and steady-state angular velocities for various mass properties as given in Table 3.

For the same four scenarios, the hydrodynamic torques on the rotor for each case are shown in Figure 12. Similar to the angular velocities (Figure 11), the average torque values over the respective steady states appear to be close to one another, while the ranges of oscillation and the time histories in the self-starting period (i.e., the first 15 s approximately) showed some variability.

The results imply that the rotors of the same geometrical configuration, but different densities would produce similar levels of power. A heavier rotor would have the benefit of smaller oscillations during the steady state, but it would also suffer from a prolonged spin-up process. For all cases in the reminder of the report, the rotor mass was set to 300 kg and the moment of inertia 120 kg·m^2 as a representative configuration.

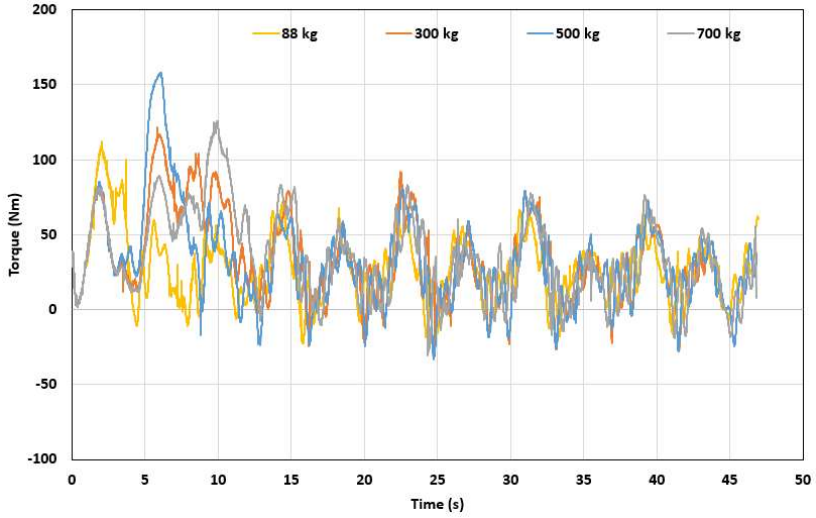

Figure 12. Transient and steady-state hydrodynamic torques on the rotor for various mass properties as given in Table 3.

7.1.4 Study of the rotational damping coefficients

As described in Section 7.1.1, the damping torque on the rotor reflects the upper limit of the useful energy that the WEC can extract from the waves. The rotational damping coefficient is hence a key design parameter that warrants further scrutiny. In this section, a wide range of damping torque coefficient values, i.e., 10, 30, 50, 70, and 90 Nms/rad, were probed to examine the rotor dynamic responses as potentially influenced by the PTO.

Table 4 presents the steady-state average angular velocity and the resistive torque for each different damping coefficient. The average values are also shown graphically in Figures 13.

Table 4. Average angular velocities and torques for various damping coefficients.

Rotational damping coefficient (Nms/rad)	Angular velocity Ω (deg/s)	Resistive Torque (Nm)
10	146.67	25.60
30	123.53	64.68
50	107.46	93.78
70	83.73	102.30
90	39.19	61.56

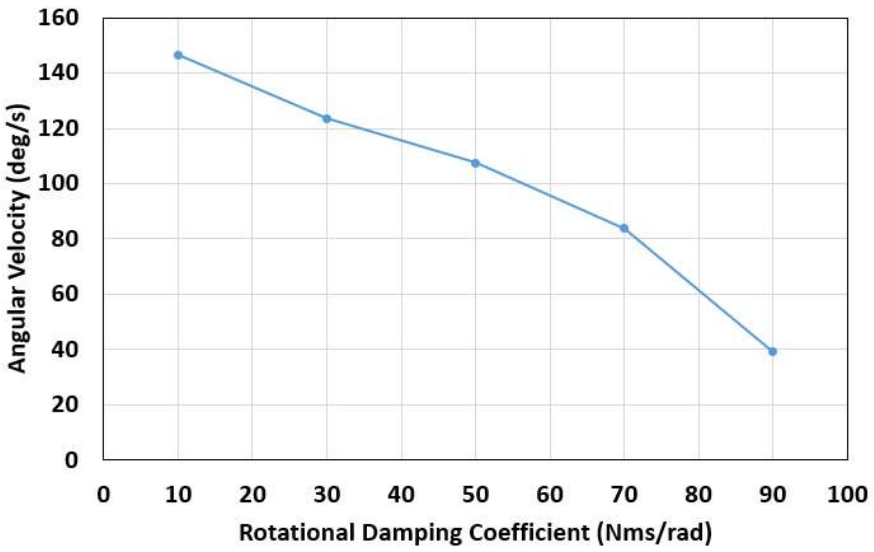

(a) Angular velocity

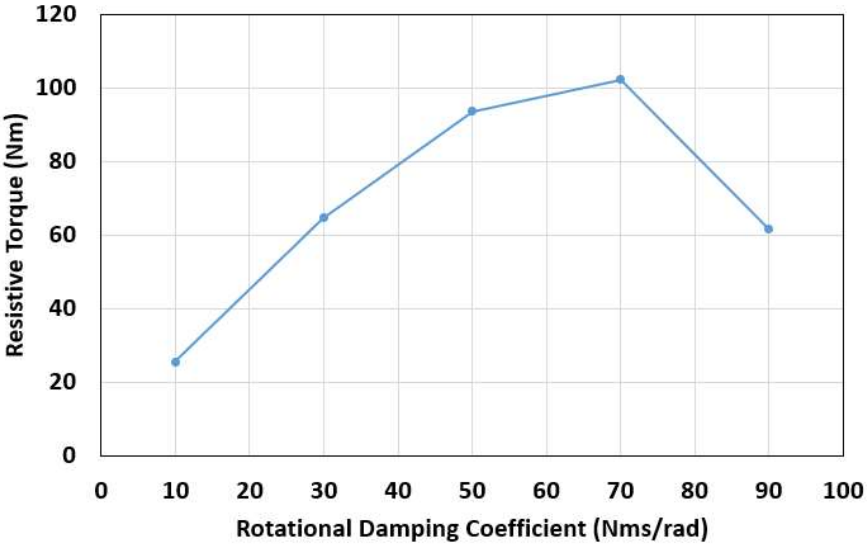

(b) Resistive torque (T_g)

Figure 13. Steady-state average angular velocity: (a) and resistive torque; (b) of the rotor with various rotational damping coefficients.

In Figure 14, the average power that was extracted through the resistive torque during the steady state peaked with a damping coefficient of 50 Nms/rad, which implies that this value of damping coefficient could provide the most power for the PTO. For the next stage simulations, the rotating damping coefficient of 50 Nms/rad was applied as a representative value.

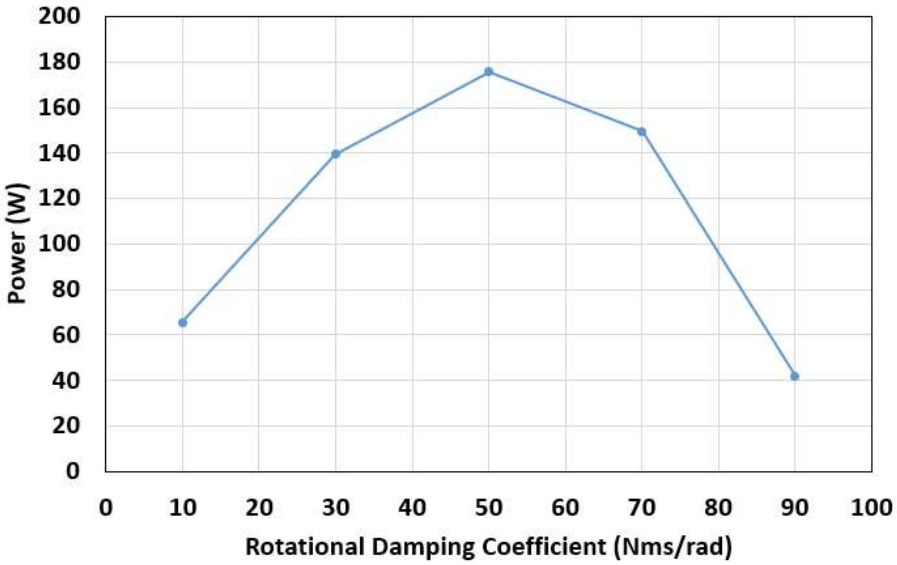

Figure 14. Extracted power ($T_g \cdot \Omega$) through the resistive torque with various rotational damping coefficients.

7.1.5 Design Variates with different Combinations of Chord Length and Horizontal Semi-axis Length

As described in Section 6.2, a test matrix based on the chord length (c) and the horizontal semi-axis length (b) was determined as shown in Table 5. A case number was assigned to each of the simulation cases; there were 12 cases in total.

Table 5. Study cases based on three different levels of chord lengths and four different levels of horizontal semi-axis lengths.

c \ b	$0.6a$	$0.8a$	$1.0a$	$1.2a$
$0.7c_0$	#5	#6	#7	#8
$1.0c_0$	#1	#2	#3 (baseline)	#4
$1.3c_0$	#9	#10	#11	#12

UTRGV provided guidance as to how these new rotor geometries were defined. The WEC rotor consisted of three curved and cambered blades. As preliminarily introduced in Section 6.2, each individual rotor blade was created by sweeping and gradually cambering an originally symmetric NACA0021 hydrofoil along a semi-elliptical guide curve. The parameters describing the semi-elliptical guide curve are defined in Figure 15, which is consistent with but more detailed than the general illustration in Figure 3. The guide curve consisted of a semielliptical arc (with a vertical semi-axis a and horizontal semi-axis b) in the middle and a straight section (with a length denoted by e) extended from the endpoint of each arc. The total length of the arc and the two straight sections is denoted by L, which is actually the total span of a rotor blade. The obtained rotor based on this guide curve would result in a swept diameter of $2R$ and a height of $2a$. For the purpose of creating geometrical variates of the rotor, the rotor height $2a$, the swept diameter $2R$, and the span L of an individual blades were held constant. Specifically for the present study, $2a = 1$ m, $2R = 4a = 2$ m, and $L = 2$ m.

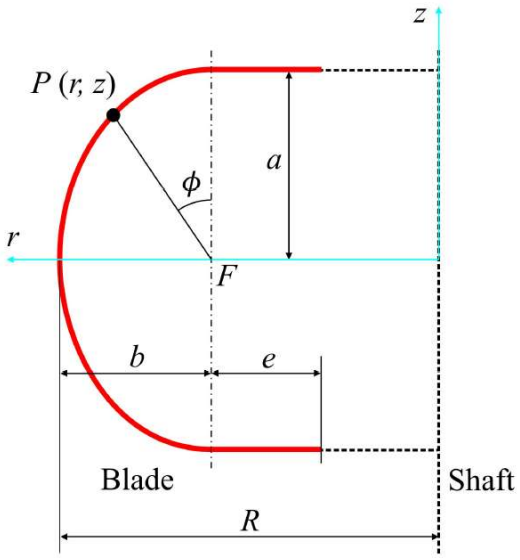

Figure 15. Definition of rotor parameters.

To form a blade, a series of two-dimensional hydrofoil profiles were first created based on a constant chord length but different cambers. The foil profiles were provided by UTRGV. Figure 16 shows an example of the foil profiles intended for different ϕ positions along the guide curve. In order to place the two-dimensional profiles in the three-dimensional space (e.g., Figure 16), ABS developed a "Rhinoscript" using Rhinoceros3D (Robert McNeel & Associates). The script was based on Visual Basic (VB) script language embedded in Rhinoceros3D, which could connect with the CAD functionalities of Rhinoceros3D seamlessly. The development of this script was a critical step in handling geometries based on mathematical formulations. When the blade profiles were placed in the three-dimensional space, each planar profile was designed to be perpendicular to the guide curve. With blade profiles in place, the blade surface was then created by the relevant functionalities of Rhinoceras3D. A complete rotor geometry was finalized by connecting individual blades to the central shaft with spokes (Figure 3). Each spoke had a diameter of 40 mm; its axis went through the maximum thickness location chordwise and the mid- thickness level at each blade end. The rotational shaft has a diameter of 80 mm and a length of 1,160 mm with rounded ends. Other minor features of the rotor were omitted in the numerical simulation for simplicity.

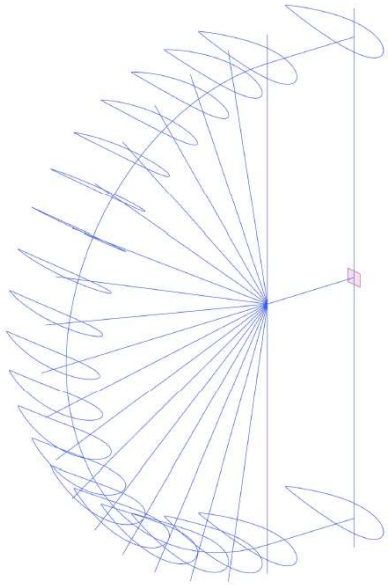

Figure 16. Two-dimensional hydrofoil profiles swept along the guide curve, with a constant chord length but varying cambers.

Blades with different chord lengths were also to be examined. Figure 17 shows the uncambered hydrofoil profiles with three different chord lengths, i.e., 0.21 m, 0.3 m, and 0.39 m. The thickness of each profile was also different in proportion to the associated chord length. Figure 18 presents the sample rotor blades generated by lofting a surface over the planar foil profiles properly positioned in the three-dimensional space with the same chord length but varying horizontal semi-axis lengths (b).

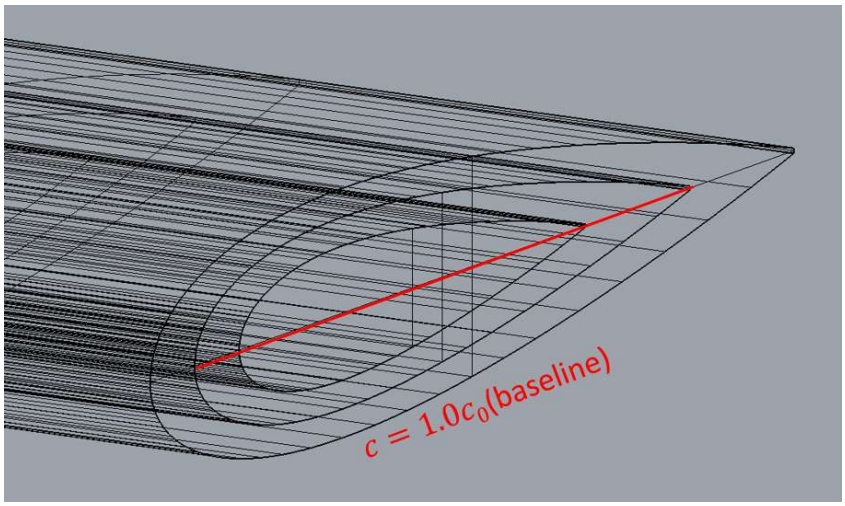

Figure 17. Three uncambered foil profiles with different chord lengths: $0.7c_0$, $1.0c_0$, and $1.3c_0$ (c_0, the baseline chord length, was 0.3 m for the present work).

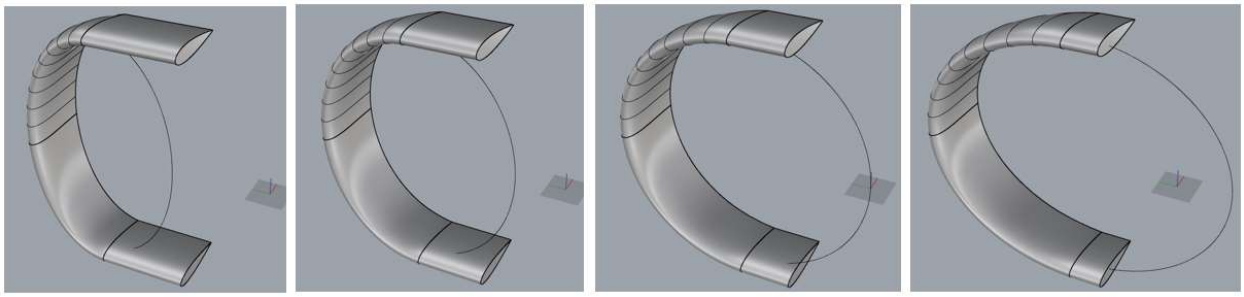

Figure 18. The rotor blades based on foil profiles with a given chord length but different guide curves.

The results obtained for the cases in Table 5 are summarized in Table 6 and graphically shown in Figure 19. It is often useful to nondimensionalize the rotational speed of the rotor into the Tip-Speed Ratio (TSR, denoted as λ), which is defined as

$$\lambda = \frac{\Omega R}{V} \tag{3}$$

In Eq. (3), V is the inflow velocity toward the rotor (taken as the maximum orbital velocity of the regular waves applied), and R is the turbine radius.

Based on the CFD results, at the geometrical parameters of $c = 1.0c_0$ and $b = 0.8a$, i.e., Case #2, yielded the maximum power among all cases in Table 6. It should be understood that the power as presented here is the rate of work done by the hydrodynamic loads to the rotor. It reflects the extra wave energy that the rotor can extract in addition to the PTO that has already been realized through the damping coefficient (50 Nms/rad). Therefore, the variate #2 was the most efficient compared to all other variates in Table 6. This design was selected for the subsequent steps.

Table 6. Summary of the simulation results for the design variates with varied chord lengths and horizontal semi-axis lengths.

Case #	b (m)	c (m)	Torque (Nm)	Ω (deg/s)	TSR	Hydro. power (W)
1	0.3	0.3	93.41	107.52	2.90	175.29
2	0.4	0.3	94.01	107.46	2.90	176.31
3 (baseline)	0.5	0.3	92.54	105.75	2.85	170.80
4	0.6	0.3	89.02	103.56	2.79	160.89
5	0.3	0.21	73.76	85.12	2.30	109.58
6	0.4	0.21	74.63	86.24	2.33	112.33
7	0.5	0.21	62.79	83.67	2.26	91.69
8	0.6	0.21	51.35	81.03	2.19	72.62
9	0.3	0.39	91.55	106.84	2.88	170.71
10	0.4	0.39	92.15	107.32	2.90	172.61
11	0.5	0.39	89.80	104.46	2.82	163.73
12	0.6	0.39	85.75	99.60	2.69	149.06

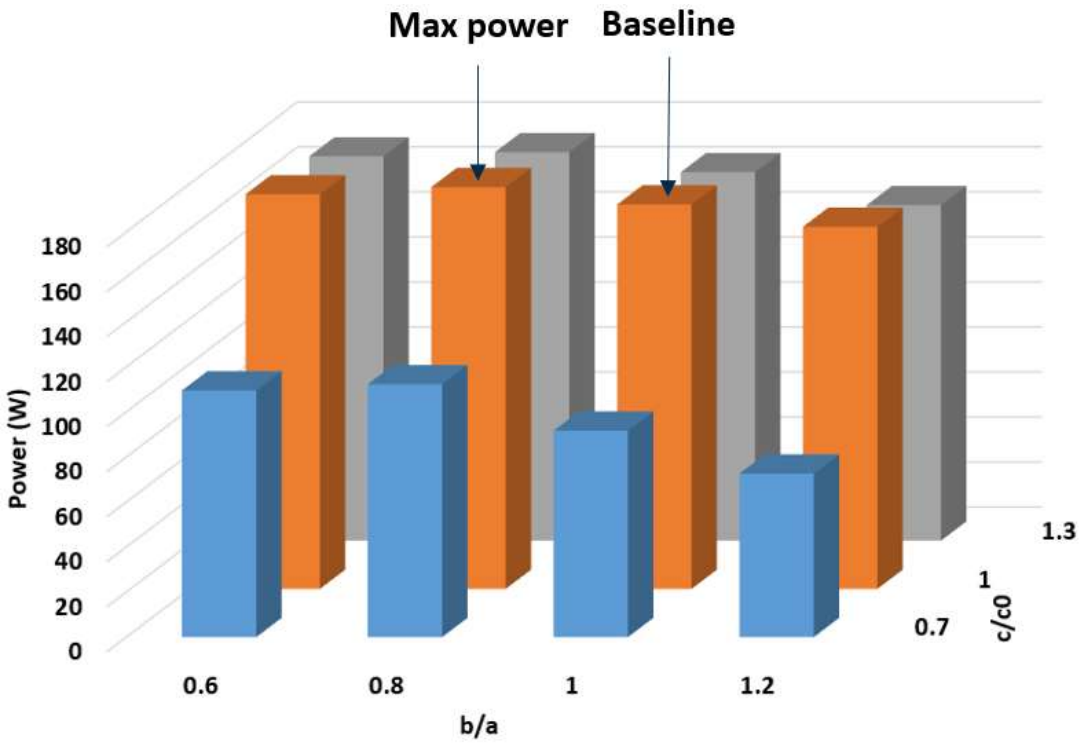

Figure 19. Comparison of the hydrodynamic power for the 12 design variates as in Table 5.

7.1.6 Effect of the Rotor Immersion Depth

Based on the results obtained in Section 7.1.5, the best design (with a chord length of $0.8a$ and a horizontal semi-axis length of $1.0c_0$) was selected for the evaluation of the effect of the rotor immersion depth on the potential hydrodynamic power. The immersion level is defined as the z-coordinate of the rotor top (0 m when the rotor top is at the static water surface). In addition to the four immersion depths described in the Test Plan (Section 6.2), three more depths, i.e., 0, 0.5, and 1.0 m, were considered. The study cases are listed in Table 7. It should be noted that all cases in the previous sections had the same immersion depth of -0.8125 m (Case L4). The rotor positions relative to the regular wave crests and troughs for typical immersion depths are illustrated in Figure 20.

Table 7. Simulation cases for evaluating the effect of the immersion depth on the hydrodynamic power of the rotor.

Case #	**L1**	**L2**	**L3**	**L4**	**L5**	**L6**	**L7**	**L8**
Immersion depth (m)	-2	-1.5	-1	-0.8125	-0.5	0	0.5	1

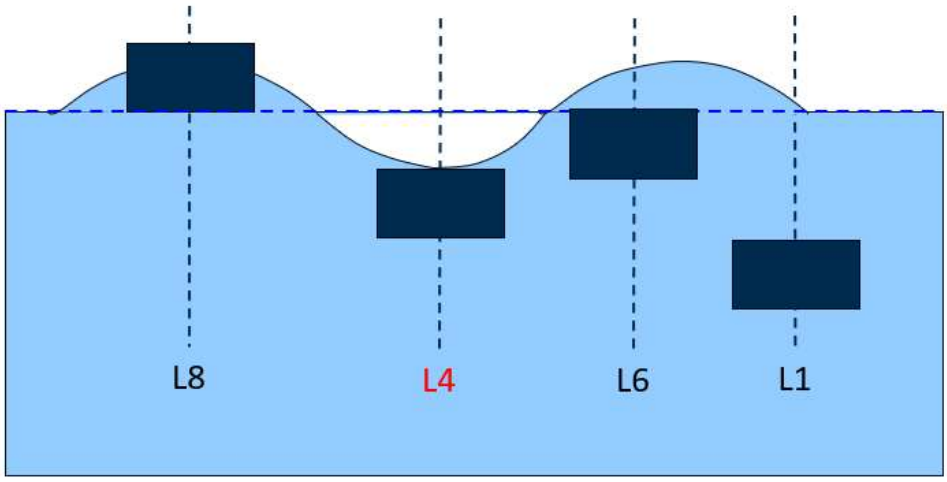

Figure 20. Four typical immersion depths for the rotor. Case L4 corresponded to an immersion depth that would allow the rotor to be just immersed underneath a wave trough; Case L6 corresponded to the immersion depth for which the rotor top would be just below the static water surface.

As an advantage of the overset grid technique, the rotor grid did not need to be re-generated. The existing rotor grid could only be shifted in the vertical direction to any desired immersion depth.

The simulation results for the cases as listed in Table 7 are summarized in Table 8. In particular, the average hydrodynamic power, average hydrodynamic torque, and average angular velocity as obtained from the steady state for each case are shown in Figure 21, Figure 22, and Figure 23, respectively.

Table 8. Simulation results for the average torque, angular velocity, and hydrodynamic power over the steady state for the cases in Table 7.

Case #	Depth (m)	Torque (Nm)	Ω (deg/s)	TSR	Power (W)
L1	-2	90.35	104.62	2.82	164.98
L2	-1.5	92.29	107.22	2.89	172.72
L3	-1	93.12	108.19	2.92	175.84
L4	-0.8125	94.01	107.46	2.90	176.31
L5	-0.5	89.26	98.93	2.67	154.11
L6	0	46.76	54.73	1.48	44.67
L7	0.5	45.68	51.93	1.40	41.40
L8	1	24.18	27.55	0.74	11.62

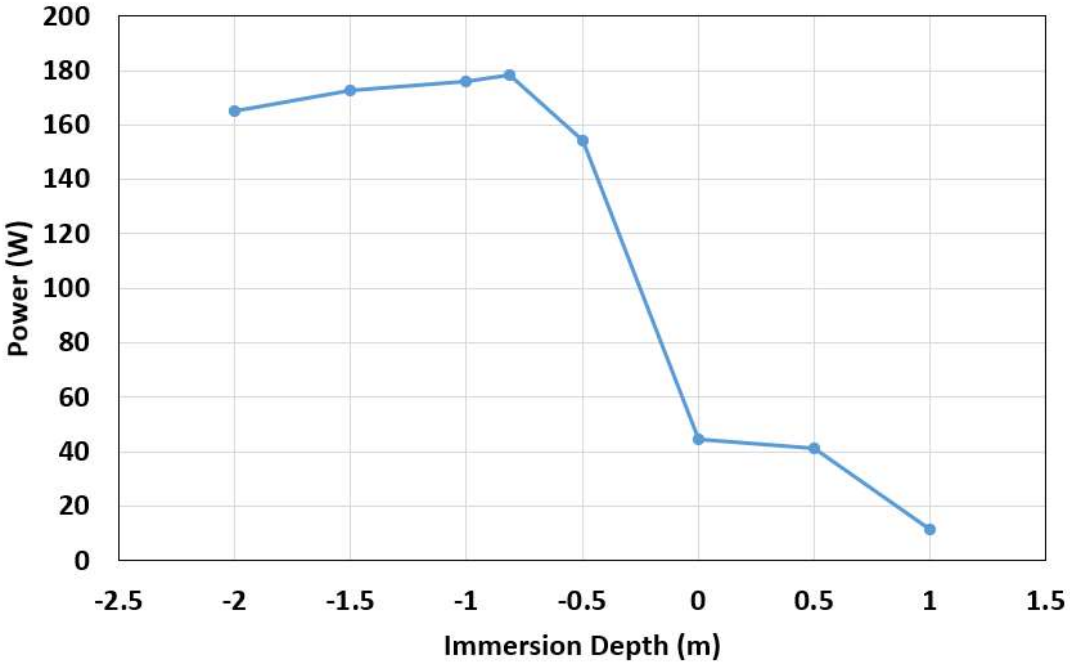

Figure 21. The rotor steady-state hydrodynamic power for various immersion levels.

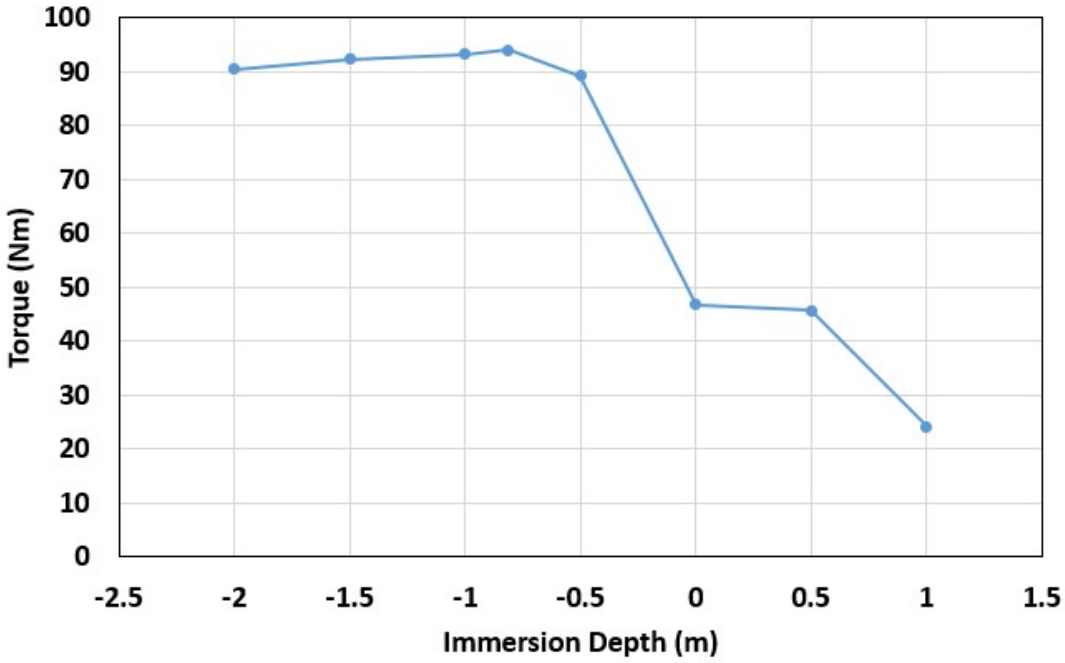

Figure 22. The rotor steady-state hydrodynamic torque for various immersion levels.

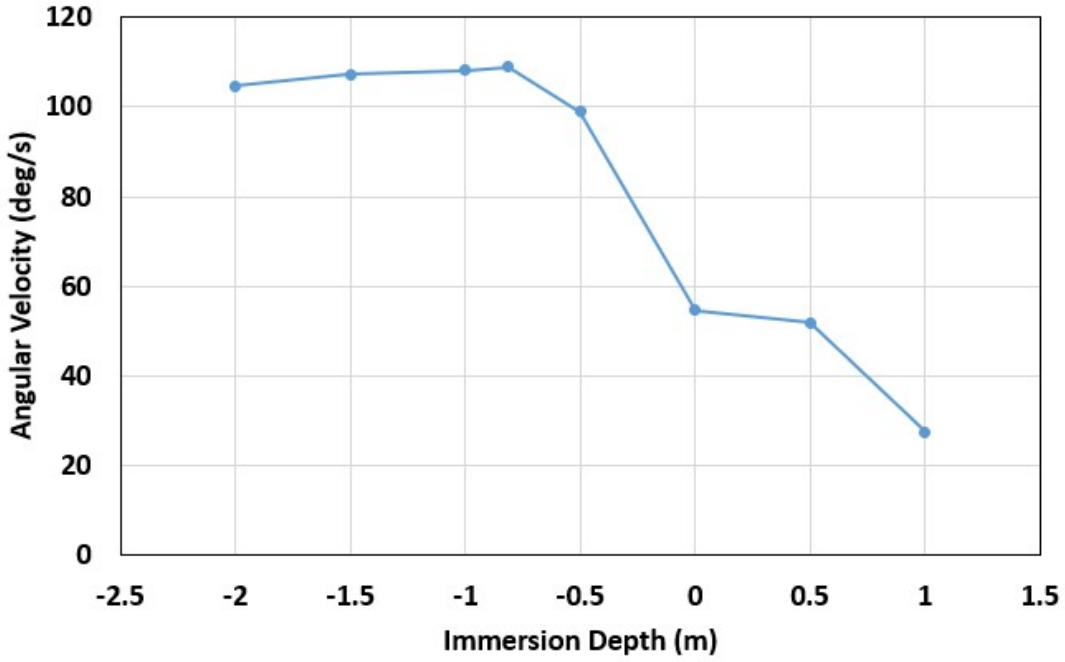

Figure 23. The rotor steady-state angular velocity for various immersion levels.

From the simulation results, Case L4 was identified to be able to provide the maximum hydrodynamic power compared to all other cases in Table 7. For this configuration, the rotor was just beneath the wave trough, as shown in Figure 20. Apparently, this level of immersion would allow the entire rotor to

receive hydrodynamic loading, rather than aerodynamic loading for part of each cycle, and at the same time keep the rotor as close to the free surface as possible. In a flow field driven by surface waves, the hydrodynamic forcing is always greatest at the free surface and decays exponentially with increasing depth. As Case L4 is selected as the best configuration among all candidates, more detailed flow field characteristics are shown for this case.

The time histories of the instantaneous angular velocity, torque, and hydrodynamic power for Case L4 are plotted in Figure 24, Figure 25, and Figure 26, respectively. Clearly, the WEC was dynamic due to the unsteady driving forces of the sea waves. Even with flow reversal in each wave cycle, the rotor was able to pick up speed successfully to maintain a steady oscillating pattern. It is also noted that the steady-state characteristics were oscillatory but not exactly periodic, perhaps due to the nonlinearity in the wave-rotor interaction. This process demonstrated the sustained positive work that the regular wave induced flow field did on the rotor.

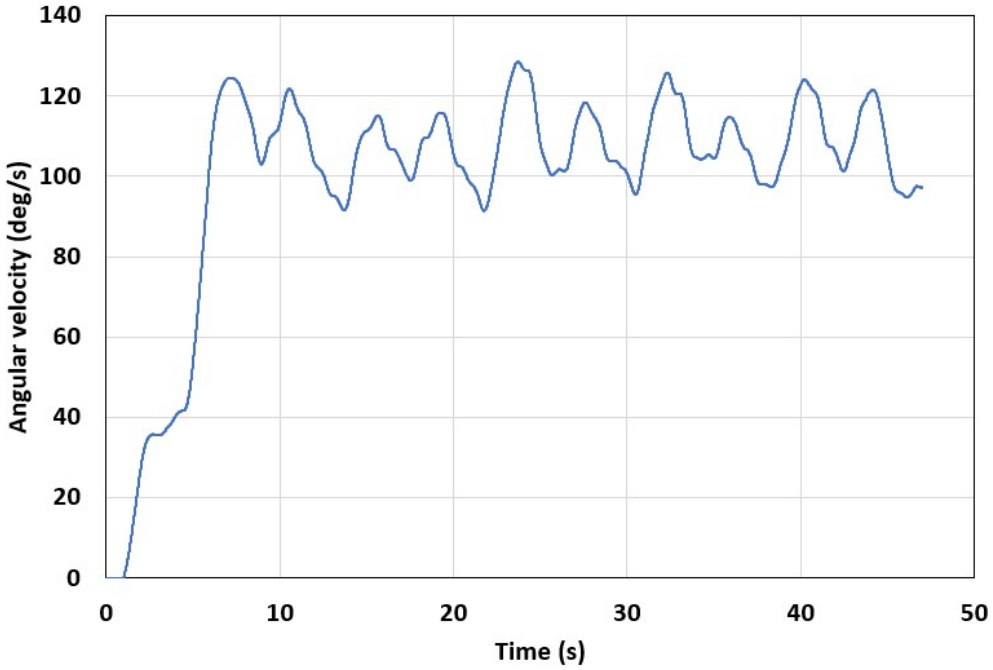

Figure 24. The instantaneous angular velocity of the rotor for Case L4.

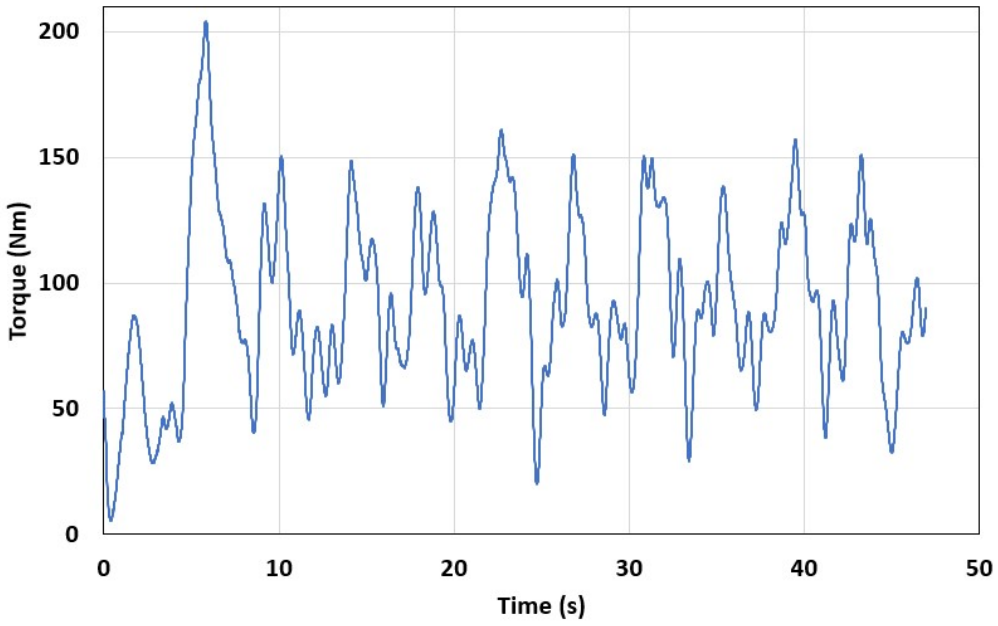

Figure 25. The instantaneous hydrodynamic torque on the rotor for Case L4.

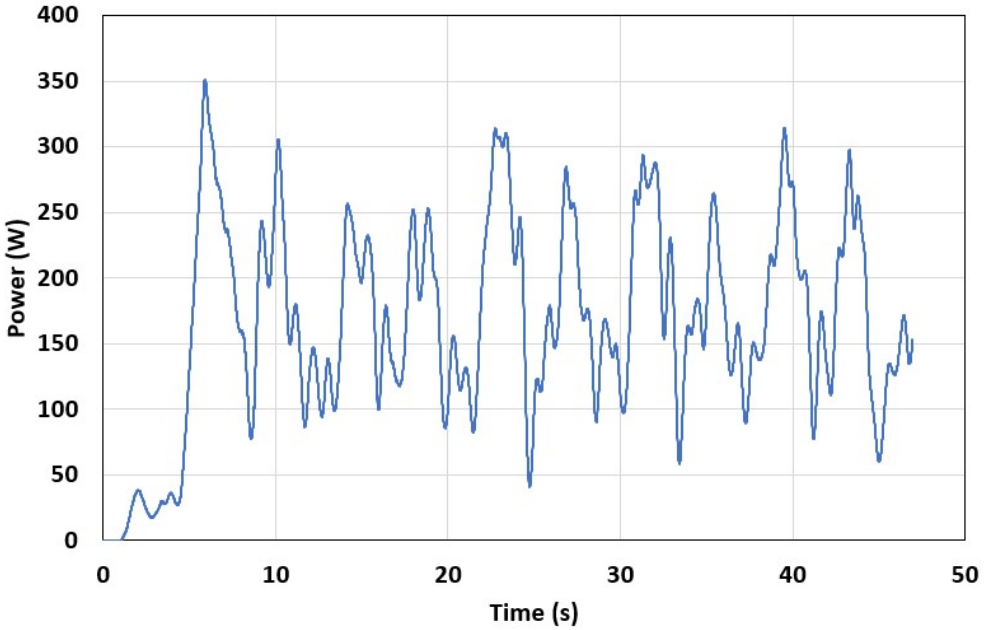

Figure 26. The instantaneous hydrodynamic power of the rotor for Case L4.

The velocity fields (Ux, the velocity component in the x-direction) and the corresponding free surface patterns at the times when wave peak or trough passed through the rotor are shown in Figure 27 shows the contour of Ux. Figure 28 presents the dynamic pressure distributions on the rotor surface at the same times as in Figure 27. Figure 29 shows the velocity fields at the same times as those for Figures 27 and 28 as viewed from above the rotor.

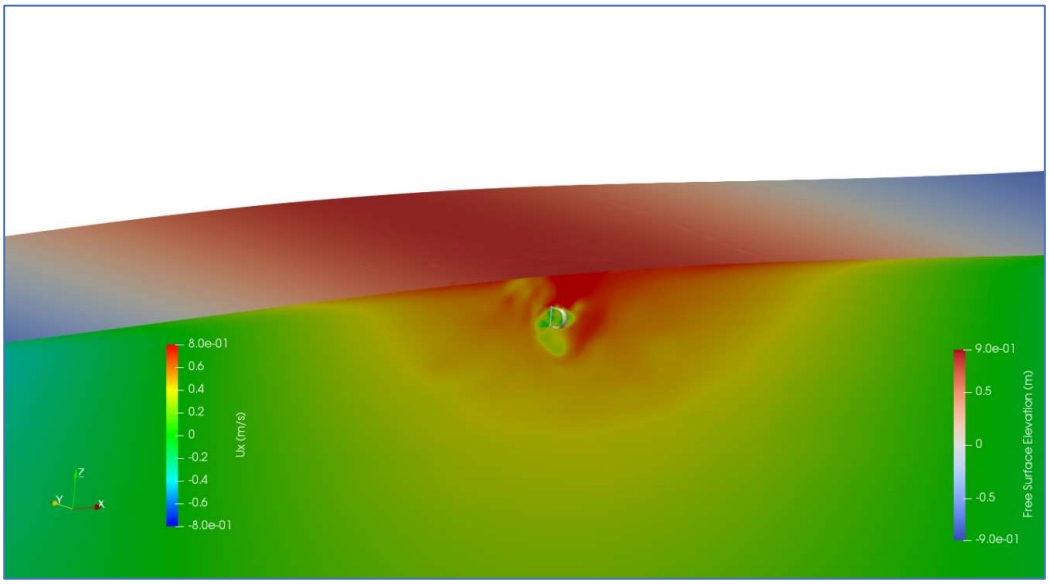

(a) Rotor at wave crest

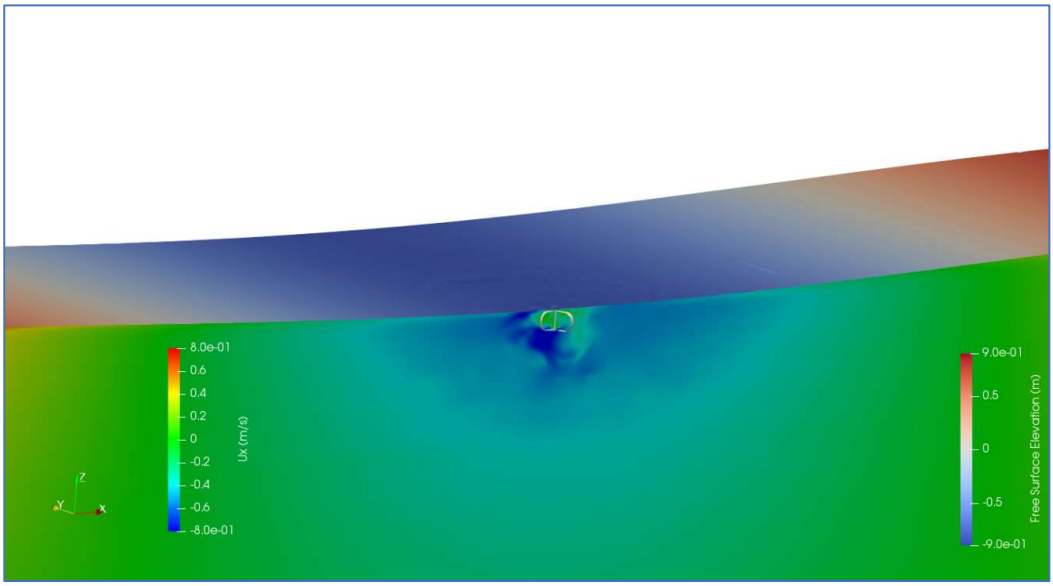

(b) Rotor at wave trough

Figure 27. Velocity field (Ux at the plane of $y = 0$) and free surface elevation patterns for Case L4: (a) rotor at wave crest; (b) rotor at wave trough.

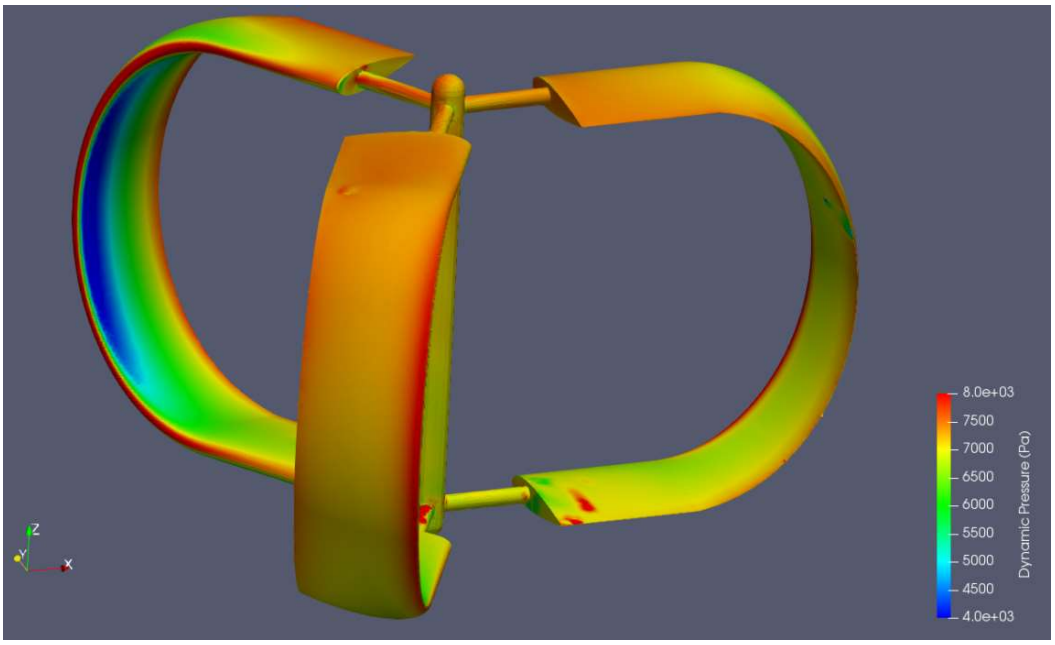

(a) Rotor at wave crest

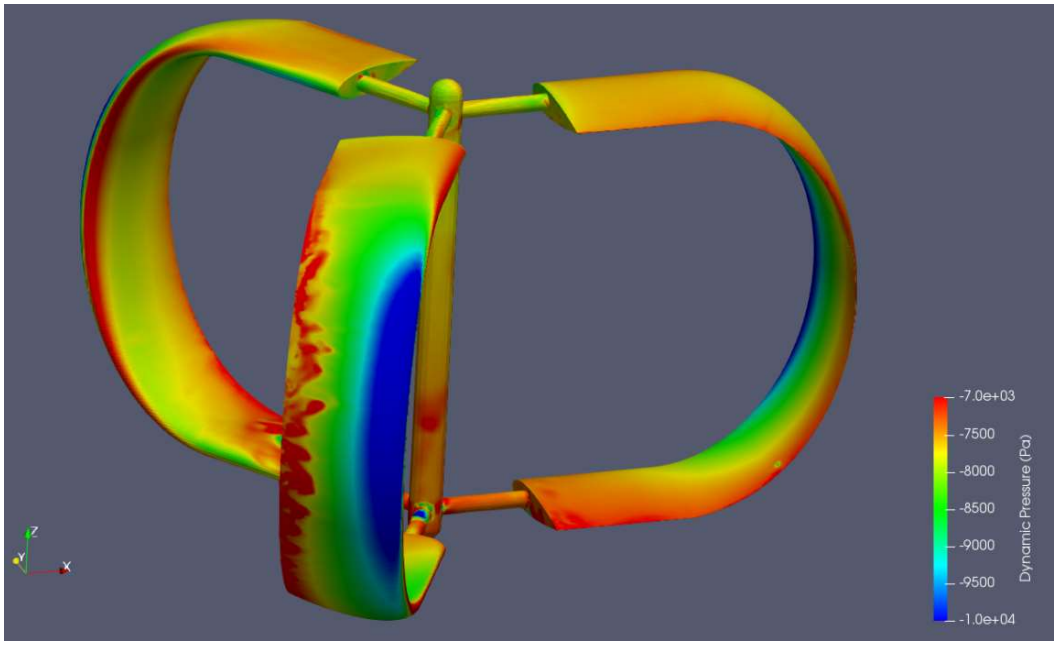

(b) Rotor at wave trough

Figure 28. Dynamic pressure distributions on the rotor surface for Case L4: (a) rotor at wave crest at the same as Figure 27(a); (b) rotor at wave trough at the same time as Figure 27(b).

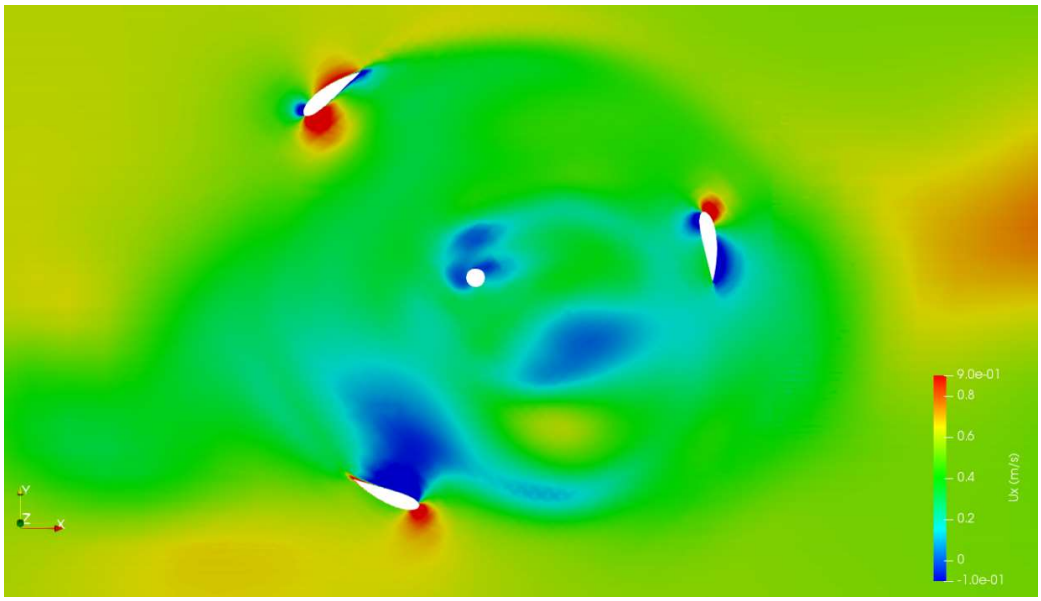

(a) Rotor at wave crest

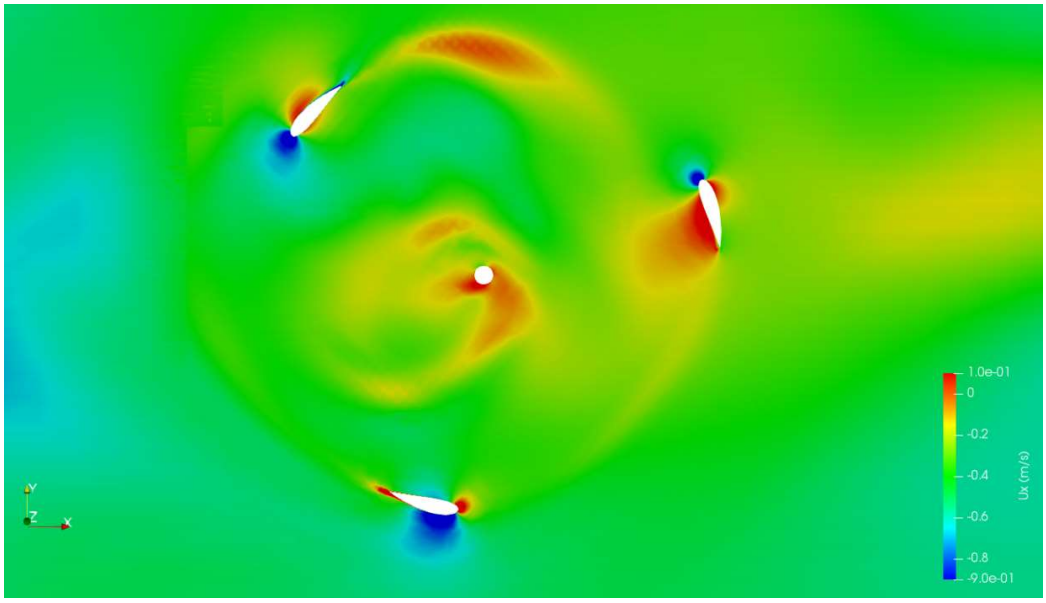

(b) Rotor at wave trough

Figure 29. Velocity field (Ux at the plane of z = -1.3125 m) for Case L4: (a) rotor at wave crest; (b) rotor at wave trough.

Figure 30 show the patterns of the z-component of the vorticity, ω_z, on a horizontal plane at z = -1.3125 m when the rotor was underneath a wave crest and a wave trough, respectively. The quantity ω_z is defined as

$$\omega_z = \frac{\partial v}{\partial x} - \frac{\partial u}{\partial y} \quad (3)$$

where u and v are velocity components in the x-direction and y-direction, respectively.

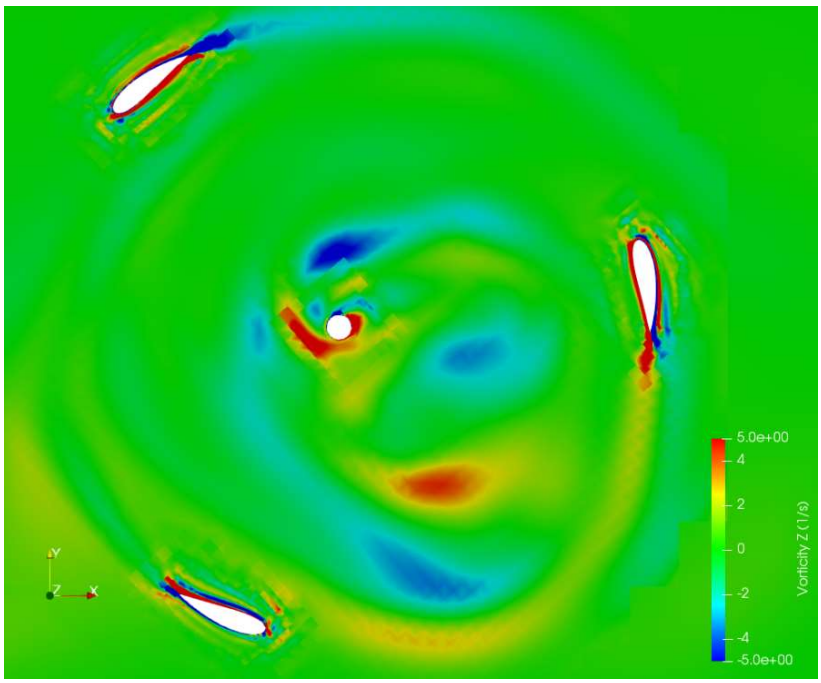

(a) Rotor at wave crest

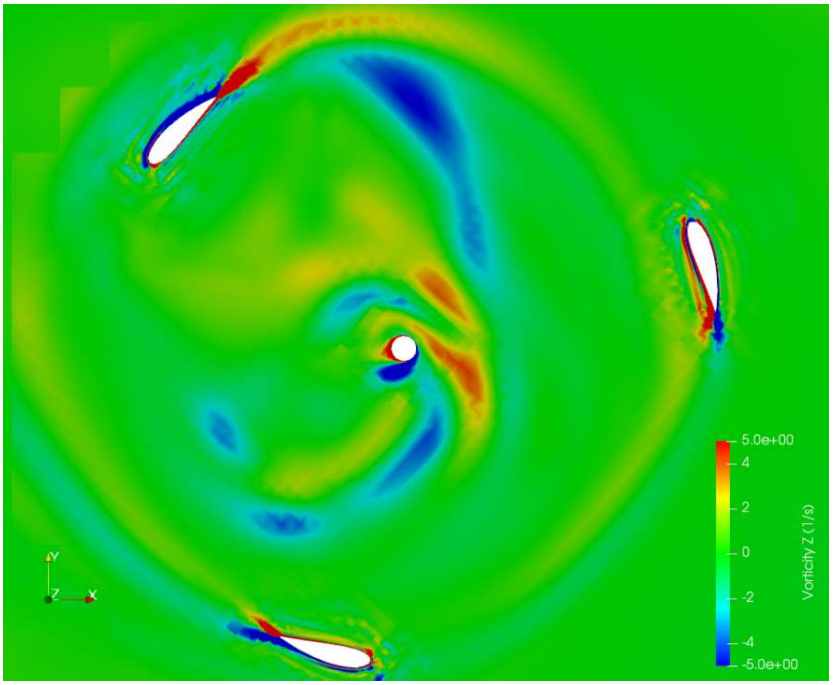

(b) Rotor at wave trough

Figure 30. Patterns of the vorticity component ω_z in a horizontal plane at z = -1.3125 m: (a) rotor at wave crest; (b) rotor at wave trough.

Figure 31 shows the iso-surfaces of the Q-criterion for the rotor at wave crest and wave trough, respectively. Two levels of the Q-criterion, i.e., 3 and 10, are presented. These iso-surfaces reveal the complex 3D vortical structures as induced by the passage of the WEC blades through the wave flow field and complement the visualization of the 2D ω_z field as shown in Figure 30. It is anticipated that the use of more advanced turbulence models such as the Detached Eddy Simulation (DES) or Large Eddy Simulation (LES) could resolve more delicate vortical structures or even eddies in the flow field.

(a) Rotor at wave crest (left: Q-criterion = 3; right: Q-criterion = 10)

(b) Rotor at wave trough (left: Q-criterion = 3; right: Q-criterion = 10)

Figure 31. Iso-surfaces of the Q-criterion for (a) rotor at wave crest and (b) rotor at wave trough.

In contrast to Case L4, Case L8 demonstrates very different patterns. This is because Case L8 would have part of the rotor emerging from the water during each wave cycle so that the rotor always lost part of the hydrodynamic forcing as compared with Case L4. Figure 32, Figure 33, and Figure 34 present the time histories of the instantaneous angular velocity, torque, and hydrodynamic power of the rotor, respectively. It is evident that the angular velocity oscillated intensively over time. The hydrodynamic torque on the rotor could become zero nearly 1/3 of the duration for each cycle, which resulted in

temporary reductions or even total losses of hydrodynamic power as shown in Figure 33 and Figure 34.

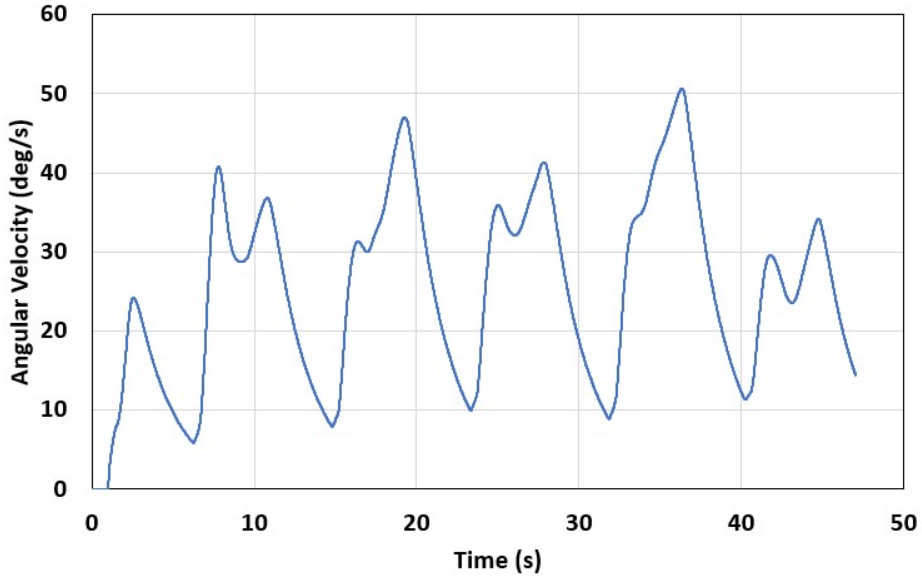

Figure 32. The instantaneous angular velocity of the rotor for Case L8.

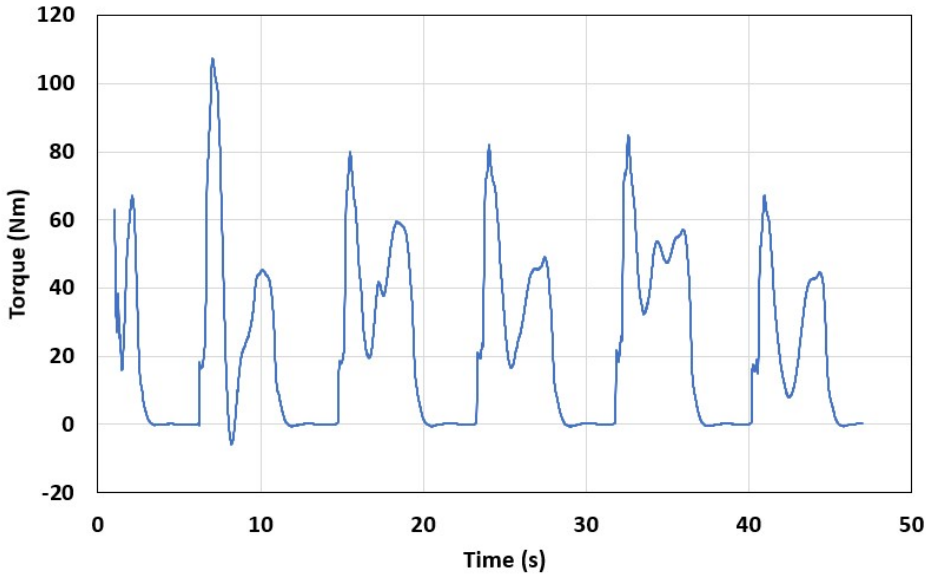

Figure 33. The instantaneous hydrodynamic torque on the rotor for Case L8.

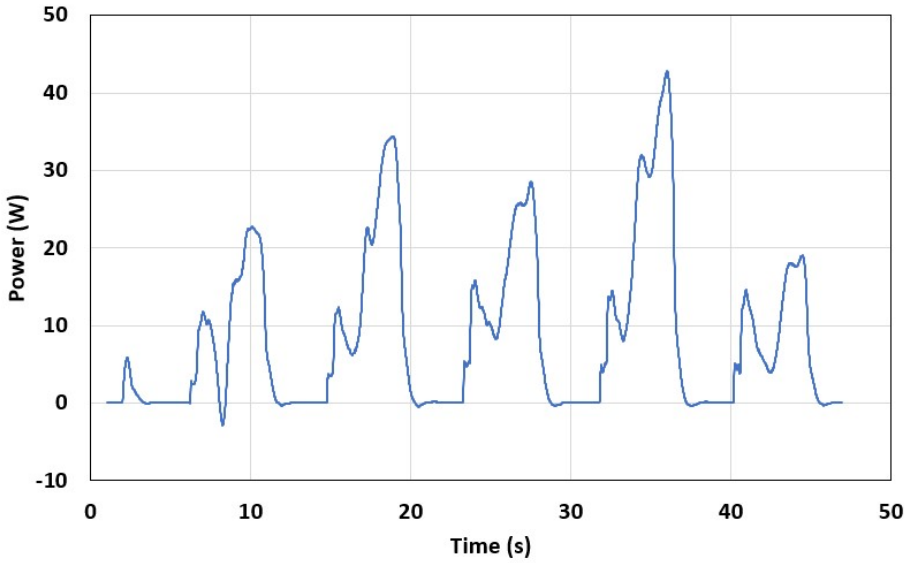

Figure 34. The instantaneous hydrodynamic power of the rotor for Case L8.

Figure 35 shows the positions of the rotor relative to the free surface when the wave crest and the wave trough arrived, respectively and the resulting dynamic pressure distributions on the rotor surface. With its particular immersion level, the rotor would be fully submerged in a wave crest but would be completely out of the water at a wave trough. This explains well why the rotor could have zero torque and power part of each cycle.

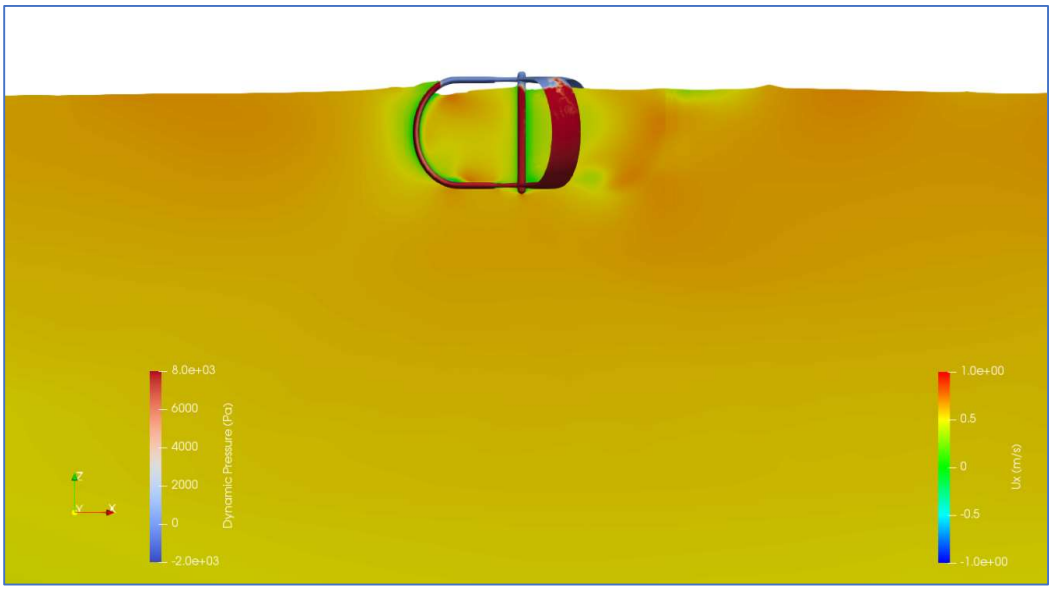

(a) Rotor at wave crest

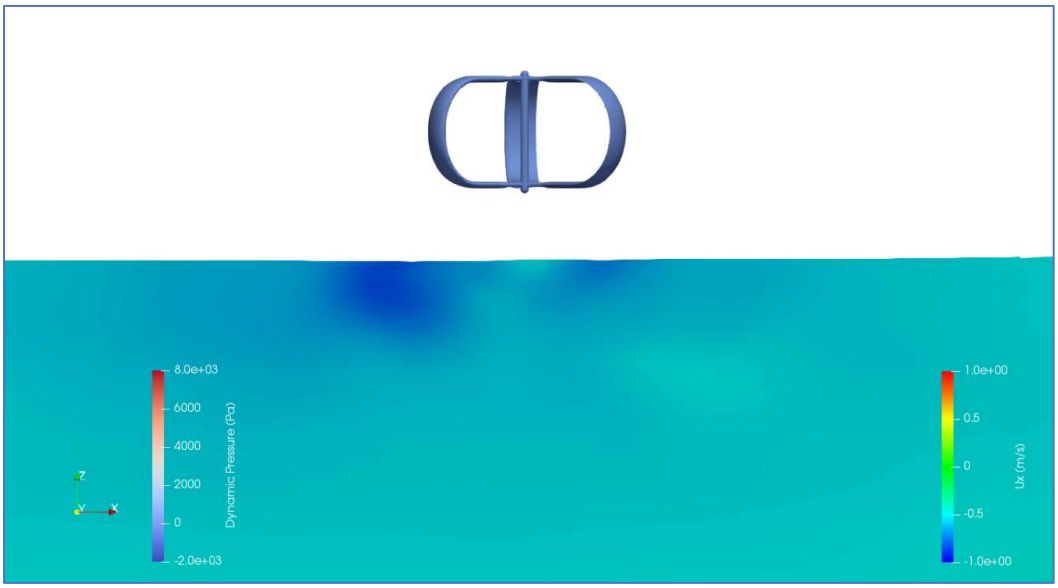

(b) Rotor at wave trough

Figure 35. Velocity fields (Ux at the plane of $y = 0$) and dynamic pressure distributions on the rotor surface for Case L8: (a) rotor at wave crest; (b) rotor at wave trough.

7.1.7 Hydrodynamic Performance of the Rotor and Single Blades

In this section, a more detailed assessment of the hydrodynamic performance of the Case L4 rotor is presented. To this end, the coefficients of torque and power, instead of the raw values as presented in previous sections, were used to reflect the hydrodynamic performance of the entire rotor or a single blade.

The torque coefficient, C_Q, and the power coefficient, C_P, are defined in the following equations

$$C_Q = \frac{Q}{\frac{1}{2}\rho A \ ^2 R} \tag{4}$$

$$C_P = \frac{\Omega Q}{\frac{1}{2}\rho A \ ^3} \tag{5}$$

Here Q denotes the torque, ρ is the water density; V is the inflow velocity (here is the maximum velocity of the water particles for the regular waves applied); R is the turbine radius; and A is the rotor's projected area which is defined as the projected area of the swept region of the rotating blades in the x-direction.

The instantaneous torque coefficient for Case L4 is shown in Figure 36, with an average value of 0.438 in the steady state. In fact, the torque coefficient time history has a high resemblance to the raw torque time history in Figure 25.

Similarly, Figure 37 shows the instantaneous power coefficient for Case L4; the average C_P value over the steady state was estimated to be 0.708.

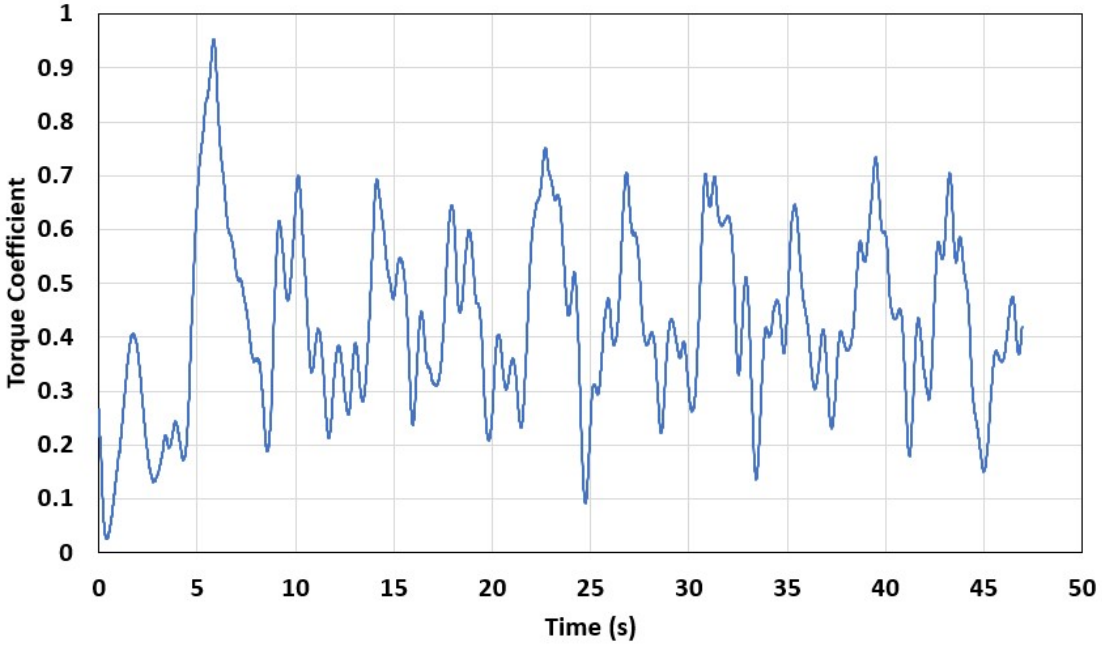

Figure 36. The instantaneous torque coefficient for Case L4.

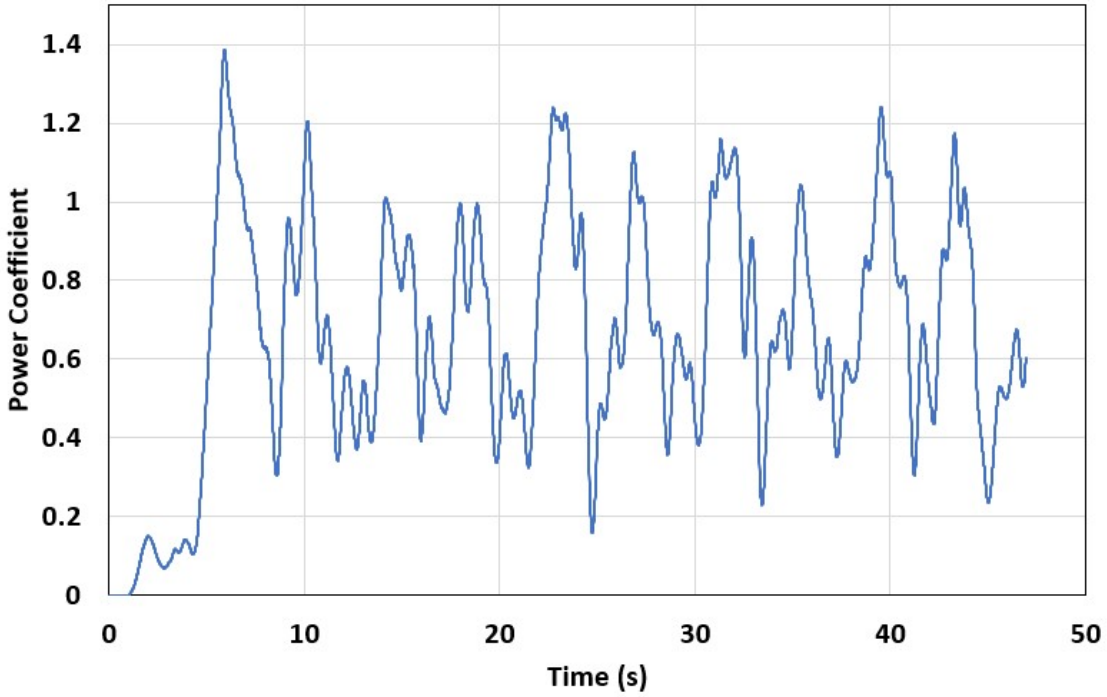

Figure 37. The instantaneous power coefficient for Case L4.

The CFD simulations also captured the instantaneous force, moment (torque), and hydrodynamic power on each single blade. The resultant force components on a blade are shown in Figure 38. The directions of the force projection, x, y, and z, are globally fixed frame of reference rather than a blade-fixed frame

of reference. It can be observed that, for a single blade, there was a phase difference between F_x and F_y, but the pattern was not pure periodic oscillations due to the non-linear interactions between the rotor blades and the incident waves. F_z, on the other hand, was more periodical, in accordance with the incident regular waves applied.

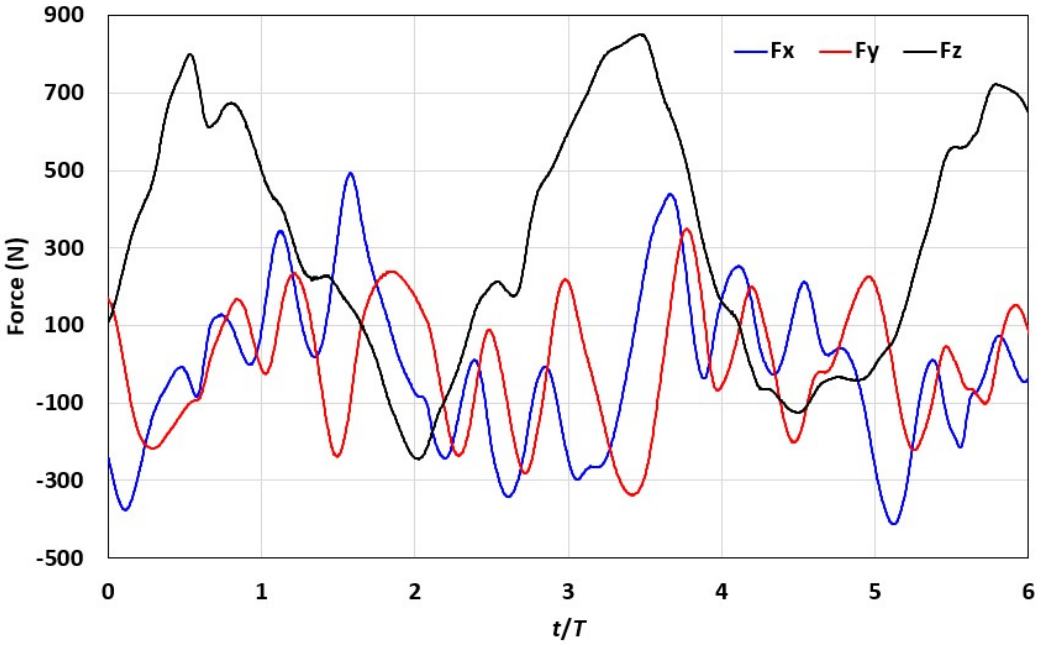

Figure 38. Instantaneous force components (F_x , F_y and F_z) on a single blade over 6 rotor revolutions for Case L4.

The resultant moment about the central rotational axis, i.e., the torque, and the hydrodynamic power of the three individual blades are plotted in Figure 39 and Figure 40, respectively. These time histories also show irregular patterns for the three individual blades due to the nonlinear effects. However, all blades appeared to show similar temporal patterns for both torque and hydrodynamic power.

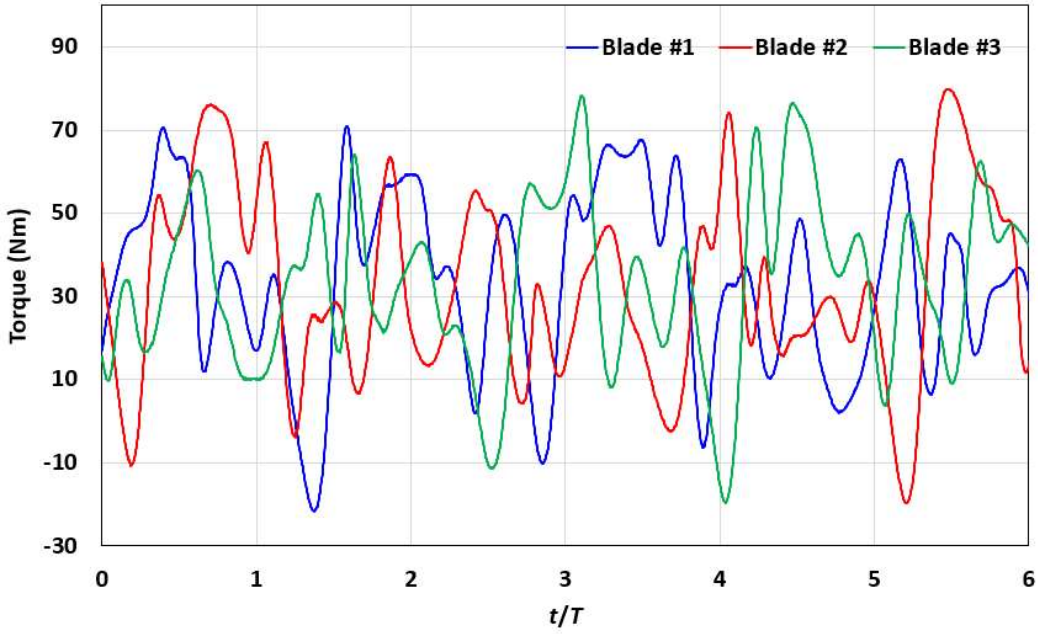

Figure 39. Instantaneous torque on each individual blade over 6 rotor revolutions for Case L4.

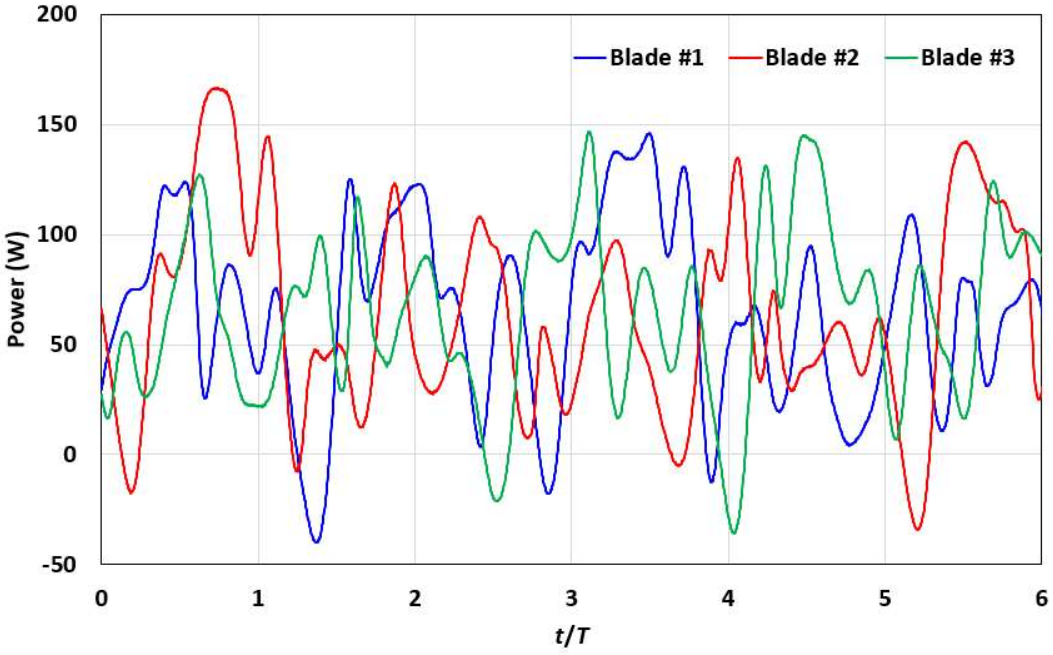

Figure 40. Instantaneous power of the individual blades during 6 rotor revolutions for Case L4.

7.2 Lesson Learned and Test Plan Deviation

In the present study, the Test Plan was well followed and there was no deviation from the original Test Plan. The project was completed by the deadline.

ABS went beyond the original Test Plan by performing three extra cases for varied immersion depths of the rotor: L6 (0 m), L7 (0.5 m), and L8 (1.0 m) (Section 7.1.6). The results from the three extra cases helped confirm the optimum immersion depth for the deployment of the rotor in the field.

8 CONCLUSIONS AND RECOMMENDATIONS

CFD was used to evaluate the energy potential of different design variates of UTRGV's baseline wave turbine model. The chord length of the rotor blades and the horizontal semi-axis length of the guide curve were perturbed to create new geometrical variates of the rotor. A CFD-based parametric study found that the optimal configuration of the rotor should:

- Have the same blade chord length as the baseline design ($1.0c_0$),
- Have the baseline horizontal semi-axis length b reduced to $0.8a$, and
- Place the rotor as close to the free surface as possible but keep the rotor submerged throughout the operation.

In the present study, the effect of the rotor total mass and the rotational damping coefficient were examined. The WEC was found to be able to self-start over a wide range of mass and damping coefficient. These dynamic characteristics will afford high flexibility in the selection of the materials, the design of the PTO, the mooring system, and the ballasting strategies for the WEC.

The findings of this study will provide invaluable insight into the directions for design modification. This will further help with the setup of a more sophisticated energy efficiency optimization in the future phases of the development.

9 REFERENCES

Khalid, M. S. U., Wood, D., Hemmati, A., 2022. Self-starting characteristics and flow-induced rotation of single- and dual-stage vertical-axis wind turbines. Energies 15 (24), 9365.

Liu, Z., Qu, H., Shi, H., 2016. Numerical study on self-starting performance of Darrieus vertical axis turbine for tidal stream energy conversion. Energies 9 (10), 789.

Omar, D. L. M., Jhon, J. Q., Santiago, L., 2018. RANS and hybrid RANS-LES simulations of an H-type Darrieus vertical axis water turbine. Energies 11 (9), 2348.

Zhu, L., Hou, E., Zhou, Q., Wu, H., 2022. Numerical experiments on hydrodynamic performance and the wake of a self-starting vertical axis tidal turbine array. J. Mar. Sci. Eng. 10 (10), 1361.

10 ACKNOWLEDGEMENTS

ABS gratefully acknowledges the financial support of TEAMER.